University of Alberta

Dynamic Behavior of Surface-bonded Piezoelectric Sensor with Interfacial Debonding

by

Hongbo Huang

A thesis submitted to the Faculty of Graduate Studies and Research
in partial fulfillment of the requirements for the degree of

Master of Science

Department of Mechanical Engineering

Examining Committee

Xiaodong Wang, Mechanical Engineering

Zihui Xia, Mechanical Engineering

Weixing Chen, Chemical and Materials Engineering

ABSTRACT

The performance of smart structures depends on the dynamic electromechanical behavior of piezoelectric sensors/actuators and the bonding condition along the interface. This thesis contents a theoretical study of the coupled electromechanical characteristics of a surface-bonded piezoelectric sensor with interfacial debonding, which is subjected to high frequency mechanical loads. A one dimensional sensor model is proposed. Analytical solutions based on the integral equation method are provided.

Numerical simulation is conducted to evaluate the effects of different parameters upon the dynamic load transfer between the sensor and the host medium. The results indicate that, the material combination, the sensor geometry, and the loading frequency, affect the load transfer significantly. The analytical solution of the elastic wave field in the host medium is obtained and used to evaluate the effects of different parameters upon the resulting wave field. The theoretical solution demonstrates the basic properties of wave propagation under current loading conditions.

ACKNOWLEDGEMENTS

Table of Contents

List of Figures

List of Symbols

c	Half length of the interfacial debonding
h	The thickness of the sensor
x, y, z	Carstesian coordinates
ω	Circular frequency of the incident wave
θ_0	Incident angle of the incident wave to the vertical line
k_L, k_T	Longitudinal wave number, transverse wave number
k_0	Apparent wave number of the incident wave
k_s	Apparent wave number of the incident wave in the sensor
c_L, c_T	Longitudinal wave speed, transverse wave speed
c_0	Surface wave speed
A^0	Amplitude of surface wave
ψ	Phase angleof surface wave
∇	Laplacian operator
Φ, Ψ	Displacement potential functions
s	Transform variable of Fourier transform
i	Squar root of -1
t	Time
$\vec{u}_{ij}$	Displacement vector
u_{ij}	Magnitude of displacement
ε_{ij}	Magnitude of strain components
u_{ij}^0	Magnitude of the displacement of the incident wave
u_{ij}^I	Magnitude of the displacement field in the host medium with free surface
ε_{ij}^I	Magnitude of the strain field in the host medium with free surface
A^I	Amplitude of u_{ij}^I
u_{ij}^s	Magnitude of the displacement field in the sensor

u_{ij}^h	Magnitude of the displacement field in the host medium
u_{ij}^τ	Magnitude of the dynamic displacement field in the host medium by τ
ε_{ij}^s	Magnitude of the strain components in the sensor
ε_{ij}^{s*}	Magnitude of the normalized strain compoments in the sensor
$\bar{\sigma}_{ij}$	Stress tensor
σ_{ij}	Magnitude of stress components
σ_{ij}^*	Magnitude of the normalized stress components
σ_{ij}^s	Magnitude of the stress induced by the sensor
σ_{ij}^d	Magnitude of the stress by interfacial debonding
σ_{ij}^f	Magnitude of far field stress in the host medium by interfacial debonding
σ_{ij}^0	Magnitude of surface stress
σ_{ij}^{d0}	Magnitude of surface stress contributed by interfacial debonding
τ	Magnitude of interfacial shear stress
D_z	Magnitude of electric displacement
E_z	Magnitude of electric field intensity
c_{ij}	Elastic constants of piezoelectric material
e_{ij}	Piezoelectric constants of piezoelectric material
λ_i	Dielectric constants of piezoelectric material
E_h	Young's Modulus of the host medium
E_s	The effective modulus of the sensor
v	Poisson's ratio of the host medium
μ	The shear modulus of the host medium
ρ_s , ρ_h	Mass density of the sensor, the host medium
q	Material combination factor
υ	Sensor geometry parameter
J_j	Bessel functions of the first kind

T_j, U_j Chebyshev polynomials of the first and the second kind

C_j Coefficients of the Chebyshev polynomials

φ Dislocation density function

κ Dynamic strain ratio for imperfect bonding case

$\kappa(y)$ Dynamic strain ratio for imperfect bonding case

V Voltage distribution along the sensor

V_{max} Maximum value of the magnitude of the voltage along the sensor

$\overline{V}$ Normalized voltage distribution along the sensor

$\overline{V}_{max}$ Normalized maximum value of the voltage magnitude along the sensor

§1 Introduction

1.1 Background

Structural Health Monitoring (SHM) is a methodology in the interdisciplinary engineering field devoted to the monitoring and assessment of structural health and durability, integrated with remote sensing, smart materials, and computer based knowledge systems to allow engineers observe the performance of the structures over time. For those large structures or special structures like aero vehicles or buried pipelines, it is impractical to perform in-service monitoring by high-in-cost traditional nondestructive testing/evaluation (NDT/NDE) techniques such as ultrasonic and eddy currents. Besides, recent incidents in the commercial aircraft industry have raised doubts over the reliability of NDT techniques to detect cracking and corrosion. While new technology generally improves sensitivity of detection techniques it is essential that they can be shown to have the appropriate detection reliability in actual use [1].

With the development of sensor systems, data acquisition, data communication and computational methodologies, instrumentation-based on-line monitoring by making use of sensors/actuators has been a widely accepted technology for in-situ monitoring and diagnosing structural health and conditions, replacing or combining with traditional nondestructive testing methods. Among the currently available options, piezoelectric sensors incarnate the superiority because they are low in cost, highly sensitive, compact/light weight, easily formed into different shapes or wired into sensor arrays. Because of the excellent dynamic response characteristics, piezoelectric SHM is widely used in elastic wave based testing, reading and analyzing the incipient information detected by surface-bonded or embedded-in piezoelectric sensors/actuators. Compared with traditional point-by-point ultrasonic wave based NDT techniques, the piezoelectric sensor/actuator SHM technique is much more time effective and suitable for

in-service testing. Elastic wave based piezoelectric SHM can be performed in forms of either passive SHM or active SHM, while the former means a SHM system with only piezoelectric sensors which just "listen to" the structure health; and the latter means a SHM system with built-in actuators "interacting with" the structure by choosing suitable monitoring signals.

The efficiency of the monitoring is demonstrated by the coupled electromechanical dynamic behavior of the system, which is not only related by the sensor/actuator properties but also those of the host structure, as well as other parameters including loading frequencies and bonding conditions. A better understanding of the resulting wave propagation in the structure is also a prerequisite for achieving the goal of elastic wave based health monitoring.

When the piezoelectric sensor/actuator is surface bonded to the host medium, high interfacial stress field may occur due to the material discontinuity [2]. The high stress concentration may lead to the reduction of the sensing/actuating ability of piezoelectric patches by undesired debonding especially in dynamic applications. Moreover, imperfect bonding between the patches and the host structure will change the phase and the amplitude of propagated waves significantly, as well as other important parameters used in monitoring techniques, resulting in false indications on the structural conditions without an efficient sensor-diagnostic process [3]. Therefore, more detailed analytical and experimental studies on the coupled dynamic behavior of surface-bonded piezoelectric layer(s) with interfacial debonding have to be performed, in order to evaluate the reliability and feasibility of surface-bonded sensor SHM systems.

Previous works have been done to study the complicated local stress field around the perfectly bonded sensor/actuators [4-8]. Recently, some researchers have studied the effects of bonding state on elastic wave generation and reception [9], as well as the dynamic behavior of the imperfectly surface-bonded sensor/actuator system [10-13].

1.2 Research Objectives

The objective of this thesis is to investigate the effects of the interfacial debonding upon the dynamic load transfer between a surface-bonded piezoelectric sensor and the elastic host medium, as well as the elastic wave propagation inside the host structure. A one dimensional sensor model will be established to simulate the coupled dynamic behavior of the system. Numerical simulation is conducted to study the effects of different loading frequencies, material combinations and sensor geometries on the dynamic electromechanical properties of the sensor under high frequency dynamic mechanical loads. The wave propagation generated by the surface-bonded sensor and the interfacial defection is studied by analytical method as well as numerical simulation.

1.3 Organization of the Thesis

The thesis is organized as follow. The current progress and relevant theories and techniques needed in modeling the sensor system are reviewed in Chapter 2. A one dimensional sensor model is established in Chapter 3, to evaluate the coupled dynamic behavior of the surface-bonded sensor system. Typical examples are provided to show the effects of the loading frequencies, material combinations and sensor geometries upon the load transfer and the sensor signals, and the results are compared between the perfect-bonding and imperfect-bonding conditions to investigate the influence of interfacial defection. In Chapter 4, the simulation of the elastic wave propagation generated by the sensor and the interfacial crack is conducted using the established one-dimension sensor model, to investigate the effects of the above parameters upon the resulting wave propagation. The basic properties of the generated wave are examined by the explicit forms near the interface and far field inside the host structure which can be analytically obtained. The last chapter, Chapter 5, summarizes the conclusions and contributions of the study and recommends some prospective topics for the future research.

§2 Literature Review

2.1 History of Piezoelectricity and Piezoelectric Devices

Piezoelectricity phenomenon is firstly demonstrated experimentally by Pierre and Jacques Curie in the year of 1880 [14] which is the coupling between the material's mechanical and electrical behaviors. Simply speaking, electrical charges can be collected on its surface when the material is under mechanical stress. Conversely, when subjected to a voltage, a piezoelectric material will produce mechanical stress or deformation. In 1882, the core of piezoelectric applications science was established by the interactive work of European scientific community, which includes the identification of piezoelectric crystals on the basis of asymmetric crystal structure, the reversible exchange of electrical and mechanical energy, and the usefulness of thermodynamics in quantifying complex relationships among mechanical, thermal and electrical variables. The work is extended in the future 25 years and the first serious application of piezoelectric took place during World War I in 1917. P. Langevin and his French co-workers developed an ultrasonic submarine transducer by gluing a mosaic of thin quartz crystals between two steel plates, which is successfully used to locate underwater objects. Their achievements lead to the rapid development of applications of piezoelectric devices.

In nature, hundreds of materials are already known to exhibit piezoelectric behavior such as bone, silk, wood, etc. The decades from 1920 to 1940 are the first generation of applications of natural piezoelectric materials. The second generation is from 1940 to 1965, during World War II, in the U.S., Japan and the Soviet Union, isolated research groups working on improved capacitor materials discovered that certain ceramic materials (prepared by sintering metallic oxide powders) exhibited dielectric constants up to 100 times higher than common cut crystals. Furthermore, the same classes of materials (called ferroelectrics) were made to exhibit similar improvements in piezoelectric properties. The discovery

of easily manufactured piezoelectric ceramics with astonishing performance characteristics naturally touched off a revival of intense research and development into piezoelectric devices, in the following highlights and curiosities but not limited to: powerful sonar, ceramic phono cartridge, piezo ignition systems, sonobuoy (a portmanteau of sonar and buoy), microphones, ceramic audio tone transducer, as well as piezo relays.

Beginning in 1965 Japanese commercial enterprises lead the pioneering work in piezoelectric device invention and patenting, by developing several types of piezoceramic signal filters, which addressed needs arising in television, radio, and communications equipment markets; and piezoceramic igniters for natural gas/butane appliances.

As time progressed to 1980, the markets for these products continued to grow, and other similarly valuable ones were found. Most notable were audio buzzers (smoke alarms, TTL compatible tone generators), air ultrasonic transducers (television remote controls and intrusion alarms) and SAW filter devices (devices employing Surface Acoustic Wave effects to achieve high frequency signal filtering) [15]. The huge commercial success has also attracted interest of many other nations in the world and efforts are taken to develop successful piezoelectric devices.

For the purpose of use, the piezoelectric materials are divided into several categories: piezoelectric crystals, piezoelectric fibers, piezoelectric ceramics and piezoelectric polymers. At present, piezoelectric ceramics and polymers have been widely used because of their versatile superiority in physical, chemical and piezoelectric characteristics over other piezoelectric materials. Compared with traditional transducers, piezoelectric ceramic and polymer sensors and actuators, for example, lead zirconate titanate (PZT) and polyvinylidene fluoride (PVDF), are compact in size and easy to tailor to suitable shapes which can be embedded in or surface attached to the host structure to perform diagnosis, and most importantly, they are low in cost which makes it economical to apply them in large scale SHM systems.

2.2 Modeling and Analysis of Piezoelectric Sensors/Actuators

In the past few decades, since the importance of the application of built-in piezoelectric sensors/actuators in smart SHM systems, the modeling and analysis of piezoelectric sensors and actuators have attracted great attention from the research community, in order to simulate the process of sensing or actuating of surface-bonded or embedded sensors/actuators.

Bailey and Hubbard firstly established a pin-force model for a thin polyvinylidene difluoride (PVF2) layer bonded to one side of a cantilever beam, with only transverse vibration considered [16]. The output force from the actuator is constantly proportional to the input voltage applied to the system. Then, analytical model for a beam-like structure with segmented piezoelectric actuators either surface-bonded or embedded has been derived [17], where the load transfer between the actuator and a Bernoulli-Euler beam is further studied with the assumption of uniform axial stress across the thickness of the actuator [18]. This actuator model is further modified by accounting for the effects of transverse shear and axial stresses in addition to the bending moment to formulate the governing moment equilibrium [19]. Then a refined actuator model in the plane stress condition is presented for a beam structure attached with symmetrically surface-bonded piezoelectric actuator patches [20-21]. An approximate dynamic model is developed to investigate the vibration response of a simply supported elastic rectangular plate excited by a piezoelectric patch of variable rectangular geometry [22]. The results demonstrate that modes can be selectively excited and that the geometry of the actuator shape markedly affects the distribution of the response among modes. A pure bending actuator-beam model is established, to describe a cantilever beam subjected to actuation of symmetrically attached actuators to the top and bottom of its surface, and activated $180°$ out-of-phase, since the sum of the axial forces by the actuators is zero. The stress changes are assumed linearly through the thickness of the actuator and the host structure. It is based on the moment equilibrium about the neutral axis [23]. A model of an arbitrary surface bonded multiple layered actuator is utilized to predict the applied

force and moment of the piezoelectric layers on a simply supported beam [24]. The equations of motion for the transverse vibrations are derived by using Timoshenko beam theory and cast in modal state space form. The forced response of the one dimensional actuator/substructure system to the piezoelectric induced loads is obtained using an assumed mode technique, which is an approximate method by representing the dynamic response of the infinite dimensional system as a finite series of spatially dependent functions, each multiplied by a time dependent generalized coordinate.

There are also many models available for piezoelectric plates in the literature. As early as 1952, an elastic plate model was presented by Mindlin [25], and it is extended to use for a two-dimensional piezoelectric plate by utilizing power series expansions [26]. The model is further modified with the use of full series expansions [27-28]. In 1991 a consistent plate model was developed by extending a one-dimensional beam model into two dimensions [29]. The classical laminated plate theory is used to model bending and extension of laminated plates induced by piezoelectric actuators [30]. In the year of 1998, a new thin piezoelectric plate model was proposed based on Kirchhoff-Love theory of thin plates [31].

For the analysis of piezoelectric shells, theories of distributed sensing and active vibration control are first proposed by Tzou [32-33], by using the multi-layered thin shell model with an integration of distributed piezoelectric sensors and actuators. A new theory on thick anisotropic composite piezoelectric shell transducer laminates is given by Tzou, by establishing a multilayered triclinic piezoelectric laminate model [34]. For piezoelectric materials applied in multiple layered structures, because of the brittleness of piezoelectric materials, debonding between interfaces of laminates is easy to appear. Recently the new piezoelectric functional graded material, which is the integration of piezoelectric material and functional graded material, has attracted the interest of theoretical researchers [35-44].

Besides, based on the classic theory of piezothermoelasticity, the general solution of three-dimensional piezothermoelastic problems is obtained by using potential functions [45-47]. Tauchert has further investigated the control of thermal

deformation of laminated piezoelectric plates [48], and Ashida has analyzed the piezoelectric laminates subjected to axisymmetric thermal loading [49]. The other typical examples include the work by Choi [50] on the transient thermal stress problem, by Qin [51] studying the mechanical response of imperfect thermopiezoelectric materials under thermal loading, and so on.

With the development of finite element modeling technique, dynamic analysis for laminated beams has been performed in details [52]. Extension of coupled Euler–Bernoulli model of sandwich piezoelectric beams is proposed by adopting a mixed variational principle and Lagrange multiplier method [53]. For complicated piezoelectric structures, finite element method is also a powerful numerical method for modeling and analyzing. A tetrahedral finite element is presented by Allik [54], for the analysis of three-dimensional piezoelectric vibration. A three-dimensional thin hexahedron piezothermoelastic element was established in 1994 [55]. A shear actuated smart structure beam element was proposed by Benjeddou and his co-workers [56]. Finite element models based on discrete layer theories are used for the coupled field analysis of laminated plates containing piezoelectric layers [57]. Moetakef has obtained closed form expressions for higher order piezoelectric tetrahedral elements [58]. Hybrid finite element models are used to perform linear or non-linear three-dimensional piezoelectric analysis [59-60].

2.3 Dynamic Load Transfer of Piezoelectric Structures

Piezoelectric based vibration control systems have been widely applied in practical use [61-63], and piezoelectric structural health monitoring has recently attracted much interest in academic community. Two main detection strategies for health monitoring of aging structures are considered: the Electro-Mechanical impedance method (EMI) for near field damage detection, and wave propagation methods for far-field damage detection [64]. The EMI method uses the electro-mechanical coupling effect of piezoelectric transducers to measure the force impedance of the structure. By comparing the impedance spectra of the damaged structure with the baseline, i.e., the impedance spectra for the pristine

structure, the damage in the structure can be assessed [65]. Among the various schemes being considered for wave Structural Health Monitoring, Lamb-wave testing has shown great promise. While Lamb-wave testing using hand-held transducers for Non Destructive Evaluation (NDE) is a well-established technology, Lamb-wave testing for SHM using surface-bonded/embedded piezoelectric sensors/actuators is a relatively new field [66]. In this work, precise mathematical modeling of transient plane and circular-crested Lamb-wave generation and sensing using surface-bonded piezos in isotropic plates is established and consequently validated by numerical methods.

The effectiveness of the sensors/actuators is the critical factor of the performance of the piezo-based SHM system. With respect to surface-bonded piezoelectric sensors/actuators, highly concentrated stress at interfaces will appear due to the material mismatches. Therefore, the local stress field near the interfaces should be studied in detail since it plays an important role in the coupled dynamic behavior between the sensors/actuators and the host structure. The interfacial defection problems have been investigated by many researchers [67-68]. Beside the distributed surface-bonded sensors/actuators, recently, some researchers have explored the feasibility of using a semi-infinite piezoelectric plate of crystals [69].

2.4 Wave Propagation in Piezoelectric Structures

In general, structural health monitoring system includes five major parts: sensing technology, diagnostic signal generation, signal processing, identification and interpretation, and integration. Nowadays, wave-based SHM methods are widely used, and these parts are all connected by the waves used as diagnosis tools. Wave-based structural health monitoring method begins in 1950s using the techniques of generating and receiving elastic waves, which requires a transmitter and receiver separately in the pitch-patch scheme, or just one having both transmitting and receiving functions with pulse-echo configuration. By analyzing the elastic waves generated and detected by the transducers/receivers, the structural integrity can be monitored by comparing the actual state of the structure with a predefined reference state. Piezoelectric materials are widely used as the

wave transducers because of their excellent dynamic response capabilities, and because they can afford large strains produced under high frequency mechanical or electrical loads. In the past decade, with the development of the ultrasonic elastic wave based testing techniques, studies on the wave generation/reception have been performed by many researchers. Conventional methods are used in the acoustic emission (AE) studies [70] and laser-based ultrasonic wave testing studies [71]. Different transducers and receivers are developed to generate and receive the waves. However, the traditional ultrasonic wave based testing techniques used in NDT usually require bulky instruments and manual interference, thus are not suitably applied directly for in-situ or in-service monitoring of the structural health.

Recently, the feasibility of using bonded piezoelectric actuators/sensors in generating and receiving elastic waves to perform continuous diagnosis of structural integrity has been studied by many researchers. Various applications in civil, aerospace, and other engineering fields have been executed [72]. Techniques have been developed in using distributed sensor arrays in an economic and effective network especially for large industry infrastructures. Experiments and studies are also performed to investigate the features of various piezoelectric materials used in measuring and generating waves as diagnostic signals [73]. Lamb waves are commonly used as diagnostic signals, named after Horace Lamb (1849-1934, a British scientist) in honor of his fundamental contributions to this subject. It is a type of ultrasonic wave propagating between two parallel surfaces of a structure. The velocity of Lamb wave depends primarily on the product of actuation frequency and the thickness of the structure. Different modes of Lamb waves with controllable patterns and shapes can be generated by surface-bonded PVDF patches [74-76]. Embedded piezoelectric sensors/actuators are also used to excite and detect elastic waves [77]. The data received from either bonded or embedded sensors contain a lot of information, and it can be easily interrupted by many factors. Especially, if the piezoelectric sensing system has defection itself, such as unexpected imperfect bonding condition in bonded sensor/actuator system, it will affect the wave propagation apparently in high frequency loading

conditions. Previous research works have been done to investigate the elastic wave propagation in a cracked medium [78], and the effect of bonding layers between the sensor/actuator and the host medium has been studied [79]. However, as mentioned in the former subsection, for the imperfectly bonded sensor/actuator system, the singular behavior of the debonding and its effect upon the resulting wave propagation has not been thoroughly studied.

2.5 Summary

In this chapter, the brief history of piezoelectric based structural health monitoring devices has been reviewed, and the focus is on the theoretical study of the piezoelectric sensor/actuator based monitoring techniques. The dynamic behavior of the system and the characteristics of the elastic waves used in the testing techniques are the essential factors determining the diagnostic ability of the system. In the commonly used surface-bonded sensor/actuator monitoring techniques, the bonding condition along the interface between the sensor/actuator and the host structures has significant influence on both the load transfer as well as the wave propagation. However, a thorough study on an infinite sensor/actuator system with interfacial defection is still on the way, and the current work aims at providing comprehensive theoretical study on this field focusing high loading frequency situations.

§3 Analysis of the Piezoelectric Sensor System

This chapter provides a comprehensive study of the coupled electromechanical characteristics of piezoelectric sensors with interfacial debonding, which are subjected to high frequency mechanical loads. Based on the developed one dimensional sensor model by Wang and Meguid in 2000, the current sensor is characterized by an electroelastic line model which is subjected to a shear load with the poling direction perpendicular to its length. Analytical solutions based on the use of the integral equation method are provided. The changes of geometry and parameters of the materials can affect the coupled electromechanical characteristics of this sensor system, as well as the elastic wave propagation along the interface and inside the host structure. Detailed numerical simulation is conducted to evaluate this effect under different loading frequencies. The study is further extended to treat the interfacial debonding between the sensor and the host medium.

3.1 Formulation of the Problem

The considered system is a homogeneous and isotropic elastic medium, with a thin sheet of piezoelectric sensor surface-bonded to it. There is a deboned area (crack) along the interface between the medium and the sensor, as illustrated in Figure 3.1. The length of the crack is denoted as $2c$, and the thickness of the sensor is denoted as h. In Figure 3.1, z axis is the poling direction of the sensor, in which electric field is usually applied or measured. The system is subjected to an oblique harmonic incident longitudinal wave with a frequency of ω and an incident angle of θ_0. The horizontal displacement of the incident wave is given by

$$\overline{u}_y^0(y,z) = A_0 * \exp[i(Ky\sin\theta_0 + Kz\cos\theta_0 - \omega t)] \quad (3.1)$$

where A_0 denotes the magnitude of the displacement, and $K = \omega / c_L$ is the wave number, with c_L being the longitudinal wave velocity.

The steady state response of the system, including displacement, stress, and strain, will involve a time factor $\exp(-i\omega t)$. For example, the real displacement can be expressed as:

$$\bar{u}_y^0(y,z) = u_y^0(y,z) \cdot \exp(-i\omega t) \qquad (3.2)$$

where $\bar{u}_y^0(y,z)$ represents the real displacement field, and $u_y^0(y,z)$ represents the magnitude. Since $\exp(-i\omega t)$ exists in all parameters, for the purpose of convenience, in the following discussions, only the magnitudes of these field variables are used to represent these field variables.

This study will focus on a thin-sheet sensor, with relatively small thickness in comparison with its length and width. Here we only consider small debonding situation, in which the boundary condition at the ends of the sensor may be ignored, so the sensor can be assumed to be infinite in length. Therefore, the magnitude of axial stress σ_y^s and strain ε_y^s can be assumed to be uniform across the thickness of the sensor, where the superscript 's' represents the sensor. Because the thickness of the sensor used is very small compared with its length, the applied electric field will mainly result in a deformation along the longitudinal direction. Accordingly, the sensor can be modeled as an electroelastic line subjected to the applied electric field and a distributed longitudinal force, $\tau(y)$, as shown in Figure 3.2, where $\tau(y)$ is the interfacial shear stress transferred between the sensor and the host structure. The longitudinal displacements of the sensor and the host medium are represented by u_y^s and u_y^h, respectively.
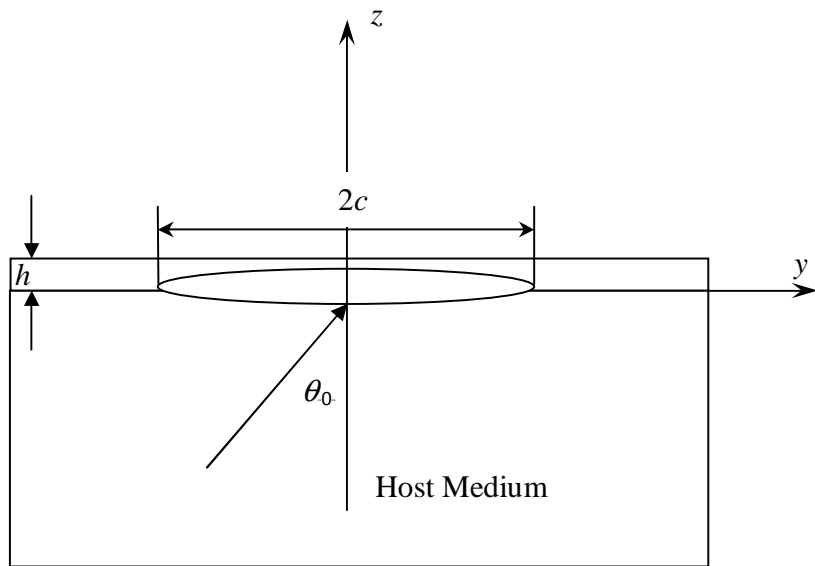
Figure 3.1: The geometry of the sensor system
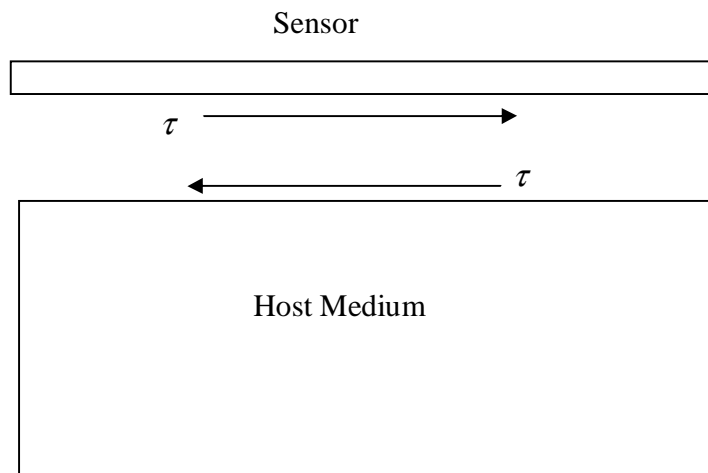
Figure 3.2: The stress field of the sensor system

3.1.1 The Dynamic Sensor Model

3.1.1.1 Electromechanical Behavior of Piezoelectric Materials

When the piezoelectric material is subjected to a mechanical load, it will produce electric displacement; and conversely, strains can be generated when electric field is applied. The former property is used in sensing, and the electromechanical behavior of piezoelectric materials can be described as:

$$\{\sigma\} = [c]\{\varepsilon\} - [e]\{E\}$$
$$\{D\} = [e]\{\varepsilon\} - [\lambda]\{E\}$$

(3.3)

where $\{\sigma\}, \{\varepsilon\}, \{D\}$ and $\{E\}$ represent the magnitude of the stresses, the strains, the electric displacement and the electric field intensity, respectively. $[c]$ is a matrix containing the elastic stiffness parameters for a constant electric potential, $[e]$ represents the piezoelectric constants, and $[\lambda]$ represents the dielectric constants for zero strains.

In the current study, for a surfaced bonded piezoelectric thin sheet with interfacial debonding, and the length of the interfacial crack is small compared with its width in the x-axis direction, it is more reasonable to consider the problem as a plane stain problem in y-z plane, which suggests that $\varepsilon_x = 0$. The surface of the piezoelectric sensor will be traction free. Therefore, the following condition should be satisfied,

$$\varepsilon_x = 0, \quad \sigma_z = 0$$

(3.4)

The stress component σ_y and the electric displacement D_z can be obtained by substituting the above equation into the constitutive equation, and the results are as follows:

$$\sigma_y = \left(c_{11} - \frac{c_{13}^2}{c_{33}} \right) \varepsilon_y - \left(e_{13} - e_{33} \frac{c_{13}}{c_{33}} \right) E_z$$

$$D_z = \left(e_{13} - e_{33} \frac{c_{13}}{c_{33}} \right) \varepsilon_y + \left(\lambda_{33} + \frac{e_{33}^2}{c_{33}} \right) E_z$$

(3.5)

where c_{11}, c_{13} and c_{33} are the elements of $[c]$, e_{11} and e_{33} are the elements of $[e]$, and λ_{33} is the element of $[\lambda]$.

Therefore, the constitutive relation of the piezoelectric material under plain deformation is given by

$$\sigma_y = E\frac{\partial u_y}{\partial y} - eE_z$$
$$D_z = e\frac{\partial u_y}{\partial y} + \lambda E_z$$

(3.6)

with the small deformation assumption

$$\varepsilon_y = \frac{\partial u_y}{\partial y}$$

(3.7)

The effective material constants of the piezoelectric materials can be expressed as

$$E = c_{11} - \frac{c_{13}^2}{c_{33}}$$

$$e = e_{13} - e_{33}\frac{c_{13}}{c_{33}}$$

(3.8)

$$\lambda = \lambda_{33} - \frac{e_{33}^2}{c_{33}}$$

3.1.1.2 The Current Sensor Model
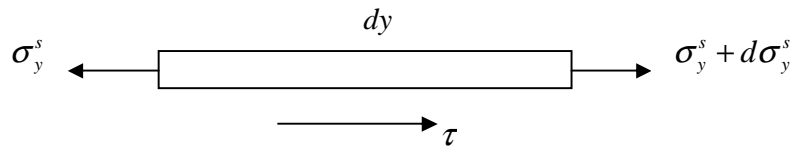
Figure 3.3: The stress field inside the sensor

The attention will be focused on cases where high frequency electric field is applied, which results in wave propagation with the typical wave length comparable to the length of the interfacial crack. In this case, the inertia effect of the sensor must be considered. According to the current one-dimensional sensor

model, the equation of motion of the sensor based on the equilibrium of force can be expressed as

$$\frac{d\sigma_y^s}{dy} + \frac{\tau(y)}{h} + \rho_s \omega^2 u_y^s = 0 \tag{3.9}$$

where the superscript and subscript 's' represent the sensor, ρ_s is the mass density of the sensor, and σ_y^s represents the magnitude of the axial stress along the sensor as shown in Figure 3.3.

In addition, the sensor will operate in an open-loop mode with no external charge supplied to it. Therefore, the electric displacement across the sensor will be zero, as $D_z = 0$. By making use of Equation (3.6), the axial stress along the sensor σ_y^s can also be expressed in terms of the axial displacement u_y^s and the electric field E_z as

$$\sigma_y^s = \overline{E}_s \frac{\partial u_y^s}{\partial y} \tag{3.10}$$

$\overline{E}_s$ is the effective modulus defined by

$$\overline{E}_s = E_s + \frac{e_s^2}{\lambda_s}, \tag{3.11}$$

where E_s, e_s, λ_s are piezoelectric material parameters.

Substitute Equation (3.10) into Equation (3.9), the governing equation of the sensor can be rewritten as

$$\frac{\partial^2 u_y^s}{\partial y^2} + k_s^2 u_y^s + \frac{\tau(y)}{\overline{E}_s h} = 0 \tag{3.12}$$

where k_s is the wave number given by

$$k_s = \omega / c_s \tag{3.13}$$

and c_s is the axial wave speed with a definition of $c_s = \sqrt{\overline{E}_s / \rho_s}$.

In order to determine the displacement and strain field inside the sensor, the governing equations can be solved using the following spatial Fourier transform,

$$\overline{f}(s) = \frac{1}{2\pi} \int_{-\infty}^{\infty} f(y) e^{isy} dy, \, f(y) = \int_{-\infty}^{\infty} \overline{f}(s) e^{-isy} ds \tag{3.14}$$

Therefore, the axial displacement and strain of the sensor can be expressed in terms of the unknown shear stress τ as:

$$\bar{u}_y^s = \frac{\bar{\tau}}{\bar{E}_s h(s^2 - k_s^2)} \tag{3.15}$$

$$\bar{\varepsilon}_y^s = \frac{-is}{\bar{E}_s h(s^2 - k_s^2)} \bar{\tau} \tag{3.16}$$

where $\bar{\tau}$, $\bar{u}_y^s$ and $\bar{\varepsilon}_y^s$ represent the Fourier transform of $\tau(y)$, the Fourier transform of the axial displacement and the Fourier transform of the axial strain, respectively.

3.1.1.3 Dynamic behavior of the host medium
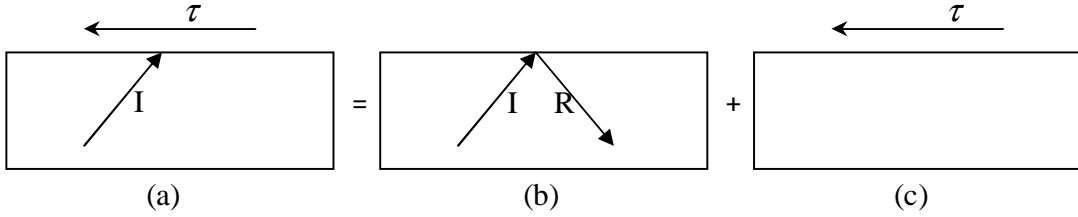
Figure 3.4: The stress field inside the host medium

The host medium is subjected to an incident wave (I) and a surface shear stress τ, as shown in configuration (a) of Figure 3.4. The incident wave will be reflected to generate a reflected wave (R) and τ will generate a dynamic field in the medium. Therefore, the stress field inside the host medium can be expressed by superimposing the configurations (b) and (c). The solution of configuration (b) can be obtained by using free-surface boundary conditions, and the corresponding displacement and strain field inside the host medium can be written as:

$$u_y^I = A^I e^{ik_0 y}$$
$$\varepsilon_y^I = ik_0 A^I e^{ik_0 y}$$

(3.17)

Here A^I and k_0 are the amplitude and the apparent wave number of the induced wave field in the configuration (b), which can be obtained by using equations (A.1) – (A.18) in Appendix A.

The unknown displacement in configuration (c) is denoted as u_y^τ, which is induced by the shear stress τ on the top surface of the host medium.

The dynamic plane strain displacement field in a homogenous isotropic elastic medium is governed by the following equations [80]:

$$(\nabla^2 + K^2)\Phi = 0, \quad (\nabla^2 + k^2)\Psi = 0$$

(3.18)

in which the Laplacian operator ∇^2 stands for $\partial^2/\partial y^2 + \partial^2/\partial z^2$, Φ and Ψ are two complex potentials, and $K = \omega/c_L$, $k = \omega/c_T$ are two wave numbers with ω, c_L and c_T being the circular frequency of the incident wave, the dilatational and shear wave velocities, respectively. The non-vanishing displacement and stress components are

$$u_y = \frac{\partial \Phi}{\partial y} + \frac{\partial \Psi}{\partial z}, \qquad u_z = \frac{\partial \Phi}{\partial z} - \frac{\partial \Psi}{\partial y} \tag{3.19}$$

The relevant stress components are

$$\sigma_y = \mu\left[-k^2\Phi - 2\frac{\partial^2\Phi}{\partial z^2} + 2\frac{\partial^2\Psi}{\partial y\partial z}\right]$$

$$\sigma_z = \mu\left[-k^2\Phi - 2\frac{\partial^2\Phi}{\partial y^2} - 2\frac{\partial^2\Psi}{\partial y\partial z}\right] \tag{3.20}$$

$$\tau_{yz} = \mu\left[2\frac{\partial^2\Phi}{\partial y\partial z} - k^2\Psi - 2\frac{\partial^2\Psi}{\partial y^2}\right]$$

where μ is the shear modulus of the isotropic elastic solid.

Therefore, the general solution of the wave induced by the shear stress τ can be determined by solving the governing equations by using the Fourier transform defined by Equation (3.14), which can be expressed as

$$\overline{\Phi}(s, z) = A(s)e^{\alpha z}, \overline{\Psi}(s, z) = B(s)e^{\beta z} \tag{3.21}$$

From which the displacement components can be determined as

$$\overline{u}_y = -isA(s)e^{\alpha z} + \beta B(s)e^{\beta z}$$

$$\overline{u}_z = \alpha A(s)e^{\alpha z} + isB(s)e^{\beta z} \tag{3.22}$$

where $A(s)$ and $B(s)$ are two unknown functions of s; and α, β are given by

$$\alpha = \begin{cases} \sqrt{s^2 - K^2} & |s| > K \\ -i\sqrt{K^2 - s^2} & |s| < K \end{cases}, \qquad \beta = \begin{cases} \sqrt{s^2 - k^2} & |s| > k \\ -i\sqrt{k^2 - s^2} & |s| < k \end{cases} \tag{3.23}$$

which ensure that the induced stress field satisfies the radiation condition of the problem at infinity.

The outgoing wave caused by τ in the host medium should satisfy the following conditions along its surface,

$$\tau_{yz} = -\tau, \qquad \sigma_z = 0 \text{ at } z = 0 \qquad (3.24)$$

Making use of the general solution of $\bar{u}_y$ and $\bar{u}_z$ and the boundary conditions, the unknown parameters $A(s)$ and $B(s)$ can be determined in terms of τ. Therefore, the Fourier transform of the dynamic displacement in the host medium u_y^τ can be expressed by

$$\bar{u}_y^\tau(s, z) = \bar{\tau} \frac{\beta}{\mu\Delta} \left[2s^2 e^{\alpha z} - (2s^2 - k^2)^2 e^{\beta z} \right] \qquad (3.25)$$

where $\Delta = (2s^2 - k^2)^2 - 4s^2 \alpha\beta$.

The Fourier transform of the dynamic stress field components cause by τ in the host medium can be obtained as

$$\bar{\sigma}_y^\tau(s, z) = \bar{\tau} \frac{2is\beta}{\Delta} \left[-(k^2 + 2\alpha^2)e^{\alpha z} + (2s^2 - k^2)e^{\beta z} \right]$$

$$\bar{\sigma}_z^\tau(s, z) = \bar{\tau} \frac{2is\beta}{\Delta} (2s^2 - k^2) \left[e^{\alpha z} - e^{\beta z} \right] \qquad (3.26)$$

$$\bar{\tau}_{yz}^\tau(s, z) = \frac{\bar{\tau}}{\Delta} \left[4s^2 \alpha\beta e^{\alpha z} - (2s^2 - k^2)^2 e^{\beta z} \right]$$

3.1.1.4. Perfectly Bonded Sensor

If the sensor is perfectly bonded to the host medium, at the upper surface of the host medium and the lower surface of the sensor, the displacement should be continuous,

$$u_y^s = u_y^I + u_y^\tau, \text{ at } z = 0 \qquad (3.27)$$

By substituting Equation (3.15) and (3.25) into Equation (3.27), the Fourier transform of τ can be expressed as

$$\bar{\tau} = \frac{\bar{u}_y^I}{m(s)} \qquad (3.28)$$

where $m(s) = \dfrac{1}{\overline{E}_s h(s^2 - k_s^2)} - \dfrac{k^2 \beta}{\mu\Delta}$.

Therefore, by substituting Equation (3.28) into Equation (3.15) and (3.16), and applying the inverse Fourier transform, the displacement and the strain field along the sensor can be obtained:

21

$$u_y^s = \frac{u_y^I}{\overline{E}_s h(k_0^2 - k_s^2)m(k_0)}, \varepsilon_y^s = \frac{\varepsilon_y^I}{\overline{E}_s h(k_0^2 - k_s^2)m(k_0)} \tag{3.29}$$

where u_y^I, ε_y^I are given by Equation (3.17), and k_0 is the apparent wave number of the incident wave.

3.1.1.5 Sensor System with Interfacial Debonding

If the sensor is not perfectly bonded to the host medium, the displacement field will be discontinuous along the interface between the sensor and the host medium. The displacement discontinuity can be expressed by the following dislocation density function:

$$\varphi(y) = \frac{\partial}{\partial y}\left[u_y^s - u_y^\tau - u_y^I\right]\Big|_{z=0} \tag{3.30}$$

By applying Fourier transform we can get

$$\overline{\varphi}(s) = -is\left[\overline{u}_y^s - \overline{u}_y^\tau - \overline{u}_y^I\right]_{z=0} \tag{3.31}$$

Therefore, the Fourier transform of the shear stress τ can be related to the deformation, by substituting Equation (3.15) and (3.25) into (3.31), as follow:

$$\overline{\tau}(s) = \frac{\overline{u}_y^I}{m(s)} + \frac{i}{s \cdot m(s)}\overline{\varphi}(s) \tag{3.32}$$

The interfacial crack is subjected to the following boundary conditions:

$$\begin{aligned}
\tau = 0, && |y| < c \\
u_y^s(y,0) = u_y^\tau(y,0) + u_y^I(y,0), && |y| \geq c
\end{aligned} \tag{3.33}$$

from which the interfacial shear stress τ can be determined.

By applying the inverse Fourier transform to Equation (3.32), the above boundary conditions can be expressed in terms of the following singular integral equations:

$$\lambda\int_{-c}^{c}\frac{\varphi(\xi)}{\xi - y}d\xi + \int_{-c}^{c}\left[\frac{1}{s \cdot m(s)} - \lambda\right]\sin[s(\xi - y)]dsd\xi = \frac{u_y^I}{m(k_0)}, \qquad |y| < c \tag{3.34}$$

and

$$\int_{-c}^{c}\varphi(\xi)d\xi = 0 \tag{3.35}$$

where $\lambda = \mu/(1-v)$ is the limit of the kernel of the integration when $s \to +\infty$, which represents the singular behavior of the field.

Equations (3.34) and (3.35) can be solved by expanding $\varphi(\xi)$ using Chebyshev polynomials as follow:

$$\varphi(\xi) = \sum_{j=0}^{\infty} C_j \frac{T_j(\xi/c)}{\sqrt{1-\xi^2/c^2}} \tag{3.36}$$

where T_j are Chebyshev polynomials of the first kind and C_j are unknown constants. From the orthogonality conditions of the Chebyshev polynomials, Equation (3.35) reduces to $C_0 = 0$. Substituting (3.36) into (3.34) and making use of the following relations $(p > 0)$:

$$\int_{-1}^{1} \frac{T_j(\xi)}{\sqrt{1-\xi^2}} \sin(p\xi)d\xi = \begin{cases} \pi(-1)^n J_j(p) & j = 2n+1 \\ 0 & j = 2n \end{cases}$$
$$\int_{-1}^{1} \frac{T_j(\xi)}{\sqrt{1-\xi^2}} \cos(p\xi)d\xi = \begin{cases} 0 & j = 2n+1 \\ \pi(-1)^n J_j(p) & j = 2n \end{cases} \tag{3.37}$$

with J_j being Bessel functions of the first kind, the following algebraic equation for C_j are obtained

$$\sum_{j=1}^{\infty} C_j U_{j-1}\left(\frac{y}{c}\right) + \sum_{j=1}^{\infty} C_j f_j(y) = \frac{u_y^l}{\lambda \cdot m(k_0)}, \qquad |y| < c \tag{3.38}$$

where U_j represent Chebyshev polynomials of the second kind with

$$f_j(y) = \begin{cases} (-1)^n \int_0^{\infty} \left[\frac{1}{\lambda \cdot s \cdot m(s)} - 1\right] J_j(sc)\cos(sy)ds & j = 2n+1 \\ (-1)^{n+1} \int_0^{\infty} \left[\frac{1}{\lambda \cdot s \cdot m(s)} - 1\right] J_j(sc)\sin(sy)ds & j = 2n \end{cases} \tag{3.39}$$

If the Chebyshev polynomials in Equation (3.36) are truncated to the Nth term and Equation (3.38) are satisfied at N collocation points given by

$$\tilde{y}_l = \frac{y_l}{c} = \cos\left(\frac{l}{N+1}\pi\right), \qquad l = 1,2,...,N \tag{3.40}$$

then Equation (3.38) reduces to the following linear algebraic equation:

$$\sum_{j=1}^{N} C_j \frac{\sin\left(\dfrac{jl}{N+1}\pi\right)}{\sin\left(\dfrac{l}{N+1}\pi\right)} + \sum_{j=1}^{N} C_j f_j(\tilde{y}_l) = \frac{\tilde{u}_y^I}{\lambda \cdot m(\tilde{k}_0)}, \qquad j,l = 1,2,...,N \quad (3.41)$$

where $\tilde{y}_l, \tilde{k}_0, \tilde{k}_s, \tilde{s}, \tilde{\beta}_s, \tilde{u}_y^I, \tilde{\varepsilon}_y^I$ are given by

$$\tilde{y} = y/c,$$

$$\tilde{k}_0 = k_0 c, \qquad \tilde{k}_s = k_s c, \qquad \tilde{s} = sc, \qquad \tilde{\beta}_s^2 = \tilde{s}^2 - \tilde{k}_s^2$$

$$\tilde{u}_y^I = \frac{A^I}{c} e^{i\tilde{k}_0 \tilde{y}} \qquad\qquad (3.42)$$

$$\tilde{\varepsilon}_y^I = \frac{A^I}{c} i\tilde{k}_0 e^{i\tilde{k}_0 \tilde{y}}$$

By solving Equation (3.41), $C_j (j=1,2,...N)$ can be determined. Therefore, the interfacial shear stress τ and the axial strain inside the sensor ε_y^s can be expressed as

$$\tau = \lambda \left\{ \frac{\tilde{u}_y^I}{\lambda \cdot m(\tilde{k}_0)} - \sum_{j=1}^{N} C_j \left[g_j(\tilde{y}) + f_j(\tilde{y}) \right] \right\}$$

$$\varepsilon_y^s = \frac{q\upsilon}{\pi} \left[\frac{\tilde{\varepsilon}_y^I}{(\tilde{k}_0^2 - \tilde{k}_s^2)\lambda \cdot m(\tilde{k}_0)} + \sum_{j=1}^{N} C_j h_j(\tilde{y}) \right] \qquad (3.43)$$

where

$$g_j(\tilde{y}) = \begin{cases} U_{j-1}(\tilde{y}) & |\tilde{y}| < 1 \\ -\dfrac{\mathrm{sgn}(\tilde{y})}{\sqrt{\tilde{y}^2 - 1}} \left[\tilde{y} - \mathrm{sgn}(\tilde{y})\sqrt{\tilde{y}^2 - 1} \right]^j & |\tilde{y}| > 1 \end{cases}$$

$$f_j(\tilde{y}) = \begin{cases} (-1)^n \displaystyle\int_0^{\infty} \left[\dfrac{1}{\lambda \cdot \tilde{s} \cdot m(\tilde{s})} - 1 \right] J_j(\tilde{s}) \cos(\tilde{s}\tilde{y}) ds & j = 2n+1 \\ (-1)^{n+1} \displaystyle\int_0^{\infty} \left[\dfrac{1}{\lambda \cdot \tilde{s} \cdot m(\tilde{s})} - 1 \right] J_j(\tilde{s}) \sin(\tilde{s}\tilde{y}) ds & j = 2n \end{cases} \qquad (3.44)$$

$$h_j(\tilde{y}) = \begin{cases} (-1)^n \displaystyle\int_0^{\infty} \dfrac{1}{\lambda \cdot \tilde{\beta}_s^2 \cdot m(\tilde{s})} J_j(\tilde{s}) \sin(\tilde{s}\tilde{y}) ds & j = 2n+1 \\ (-1)^n \displaystyle\int_0^{\infty} \dfrac{1}{\lambda \cdot \tilde{\beta}_s^2 \cdot m(\tilde{s})} J_j(\tilde{s}) \cos(\tilde{s}\tilde{y}) ds & j = 2n \end{cases}$$

with

$$q = \frac{\pi\lambda}{\overline{E}_s} = \frac{\pi E}{2(1-v^2)\overline{E}_s} \qquad (3.45)$$

$$\upsilon = c / h \qquad (3.46)$$

3.2 Analysis and Discussion

This section will be devoted to the discussion of the dynamic load transfer from the host medium to the surface-bonded sensor under different geometric and loading conditions. A longitudinal wave will be introduced as the mechanical load, and numerical simulation will be conducted to investigate the effect of the following three parameters upon the strain distribution along the sensor: the loading frequency kc, the material combination factor q as defined in (3.45), and the crack geometry υ expressed by (3.46).

Two types of sensors are considered, lead zirconate titanate (PZT-4) and polyvinylidene fluoride (PVDF) sensors. The material constants of the PZT-4 sensor and the host medium are assumed to be [81]:

Sensor (PZT-4):

$c_{11} = 13.9 \times 10^{10} Pa, \qquad c_{13} = 7.43 \times 10^{10} Pa, \qquad c_{33} = 11.5 \times 10^{10} Pa$

$e_{31} = -5.2 C / m^2, \qquad e_{33} = 15.1 C / m^2, \qquad e_{15} = 12.7 C / m^2,$

$\lambda_{11} = 6.45 \times 10^{-9} C / Vm, \qquad \lambda_{33} = 6.45 \times 10^{-9} C / Vm.$

Host Medium:

$E = 2.74 \times 10^{10} Pa, \qquad v = 0.3.$

It results in the material mismatch factor $q = 0.54$.

For the PVDF sensor and the host medium, the material constants are as follows [82], which leads to a value of $q = 20.4$.

Sensor (PVDF):

$c_{11} = 3.61 \times 10^9 Pa, \qquad c_{13} = 1.4 \times 10^9 Pa, \qquad c_{33} = 1.63 \times 10^9 Pa$

$e_{31} = 7.68 \times 10^{-3} C / m^2, \qquad e_{33} = -30.7 \times 10^{-3} C / m^2, \qquad e_{15} = -11.5 \times 10^{-3} C / m^2,$

$\lambda_{11} = 0.061 \times 10^{-9} C / Vm \qquad \lambda_{33} = 0.067 \times 10^{-9} C / Vm.$

Host Medium:

$$E = 19.5 \times 10^{10} \, Pa, \quad v = 0.28.$$

For the sake of convenience, in the following calculations, the incident angle of the incident longitudinal wave is chosen as $\theta_0 = 30°$; Poisson's ratio of the host medium $v = 0.3$; the mass density of the sensor ρ_s and the host medium ρ_h is chosen as the same, $\rho_s = \rho_h = 2700 kg / m^3$ [79].

3.2.1 Model Validation

In order to validate the current model, the finite element method (FEM) has been used, based on the static coupled-field analysis performed by the ANSYS software, by using the following loading condition: in the interfacial deboning area along the interface between the sensor and the host medium, the distributed shear stress τ with a uniform magnitude is applied. In the FEM model, twenty nodes are created across the thickness of the sensor.

Figure 3.5 shows the magnitude of the longitudinal strain of the sensor ε_y^s induced by τ along the interface between the sensor and the host medium, using the numerical method based on the current model, in comparison with the corresponding FEM results. Here the strain has been normalized by $\varepsilon_y^{s*} = \dfrac{\varepsilon_y^s}{v \cdot \varepsilon_0}$,

with $\varepsilon_0 = \dfrac{\tau}{\mu(1+v)}$ and $v = 20.0$, where v is defined by (3.46). The anisotropic elastic stiffness matrix components of the lead zirconate titanate (PZT-4) sensor are:

$$c_{11} = 13.9 \times 10^{10} \, Pa, \quad c_{12} = 7.78 \times 10^{10} \, Pa, \quad c_{13} = 7.43 \times 10^{10} \, Pa,$$
$$c_{33} = 11.5 \times 10^{10} \, Pa, \quad c_{44} = 2.56 \times 10^{10} \, Pa, \quad c_{66} = 3.06 \times 10^{10} \, Pa$$

The material constants of the host medium are [81]:

$$E = 2.74 \times 10^{10} \, Pa, \quad v = 0.3.$$

The main difference between these results occurs in the vicinity of the interfacial crack tips when *y/c* is close to -1, in which the mechanical field becomes complicated due to the high stress concentration. In other areas far away from the

crack tips, the difference is less than 2%. Therefore, the current model is validated and can be used for the current analysis.
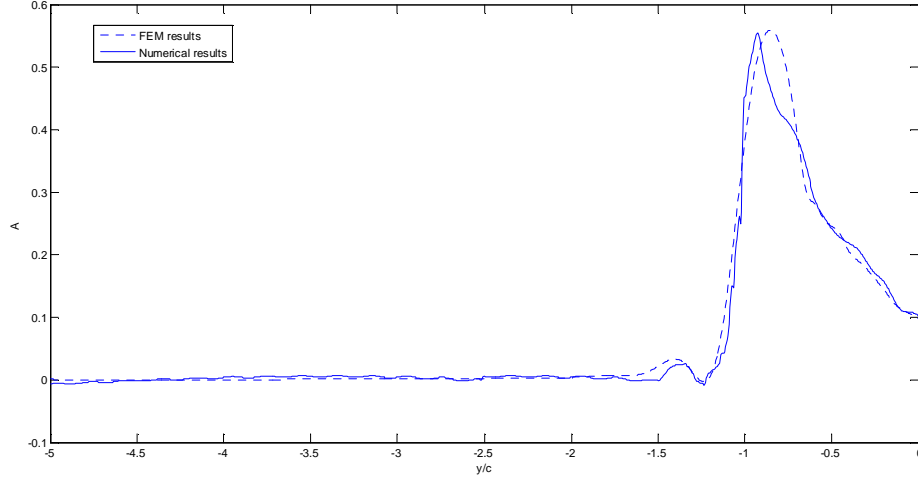
Figure 3.5: Amplitude of ε_y^{s*}

3.2.2 Strain Distribution

As shown in Figure 3.3 (a), if there is no bonded sensor on the surface of the host structure, the strain field of the medium will be $\varepsilon_y^I(y)$. Because of the existence of sensor, the strain field in the medium will be disturbed by the electromechanical coupling between the host medium and the sensor. In order to study the relation between sensor response and the undisturbed deformation, the following dynamic strain ratio $\kappa(y)$ is introduced:

$$\kappa(y) = \frac{\varepsilon_y^s(y)}{\varepsilon_y^I(y)} = A e^{i\theta},\tag{3.47}$$

where A and θ denote the amplitude and the phase angle of the dynamic strain ratio.

The dynamic strain ratio represents the percentage of deformation transferred from the host medium to the sensor. It is an index of the sensing characteristics of the piezoelectric sensor. In this section, the effect of different material properties of the sensor and the host medium, the interfacial crack geometry, and the loading

frequency upon it will be discussed. Special examples will be given in both perfect-bonding and imperfect-bonding cases.

3.2.2.1 Perfectly Bonded Piezoelectric Sensor

For the case of a perfectly-bonded sensor system which is subjected to an incident longitudinal wave as the mechanical load, the dynamic strain ratio is constant along the interface. The strain in the sensor is given by Equation (3.29), so the strain ratio can be obtained by substituting Equation (3.29) into (3.47),

$$\kappa = \frac{1}{\overline{E}_s h(k_0^2 - k_s^2) m(k_0)} = \frac{1}{1 - \overline{E}_s h(k_0^2 - k_s^2) \dfrac{k^2 \beta_0}{\mu \Delta_0}} \tag{3.48}$$

where $\beta_0 = -i\sqrt{k^2 - k_0^2}, \Delta_0 = (2k_0^2 - k^2)^2 - 4k_0^2 \sqrt{k^2 - k_0^2} \sqrt{K^2 - k_0^2}$.

For the static case where the loading frequency $k = k_0 = k_s = 0$, from Equation (3.48) we can obtain the strain ratio as 1. Figure 3.6 and Figure 3.7 show the influence of the loading frequency kh on the amplitude A and the phase angle θ of the dynamic strain ratio κ for the cases when $q = 0.5, 1.0, 2.0, 5.0$ and 20.0. With the increase of the loading frequency, the amplitude of the strain ratio decreases gradually. Besides, from Figure 3.6 and Figure 3.7 it can be observed that when q reaches 5.0 or higher, the curves are close and change with q insignificantly. The result indicates that, in the perfectly bonded case, the influence of the loading frequency on the load transfer is significant only when the loading frequency is very high. For relatively low frequency, $kh < 1.0$ for example, the change of A and θ in comparison with the static values is less than 5%.

As defined in Equation (3.45), the material mismatch factor q is an index of the relative stiffness of the sensor, representing the material combination of the sensor and the host medium. Figure 3.8 and Figure 3.9 show how the amplitude and phase angle of the dynamic strain ratio change with the material combination factor q, with a series of kh values considered. From Figure 3.8 we can see that the amplitude of the dynamic strain ratio will increase to the maximum value 1.0, when q reaches a critical value q^c about 0.3; and then diminish with the increase

of q. This critical value of q^c is independent on the loading frequencies, and it is determined by the phase angle of the incident longitudinal wave and Poisson's ratio, which can be expressed by solving the equation of $\kappa = 1$:

$$q^c = \frac{\pi(1-v'^2)\sin^2\theta_0}{2}$$

(3.49)

where θ_0 is the incident angle of the incident longitudinal wave, and $v' = \dfrac{v}{1-v}$.

For $\theta_0 = 30°$ and $v = 0.3$, $q^c = 0.31$. From the figure we can also see that under the higher loading frequency condition, the material combination affects the dynamic load transfer more significantly.
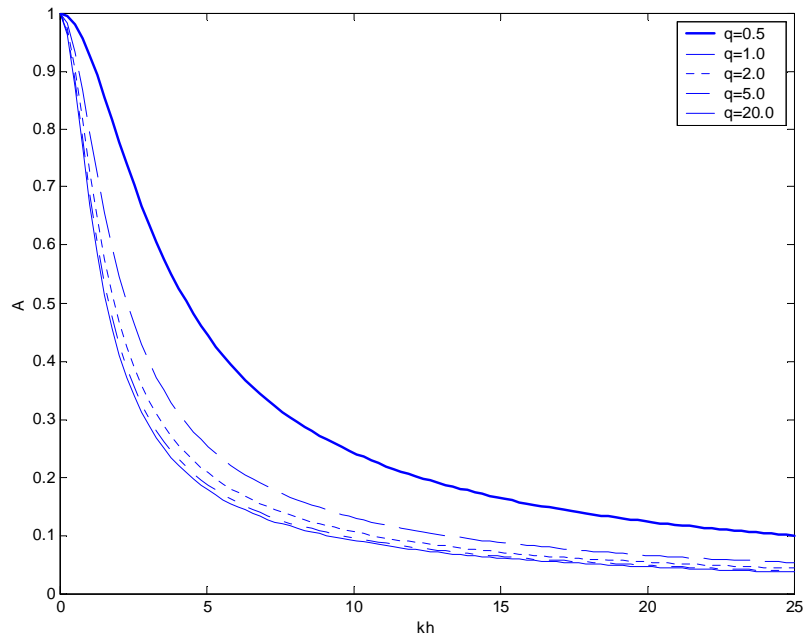
Figure 3.6: Amplitude of κ with different loading frequencies
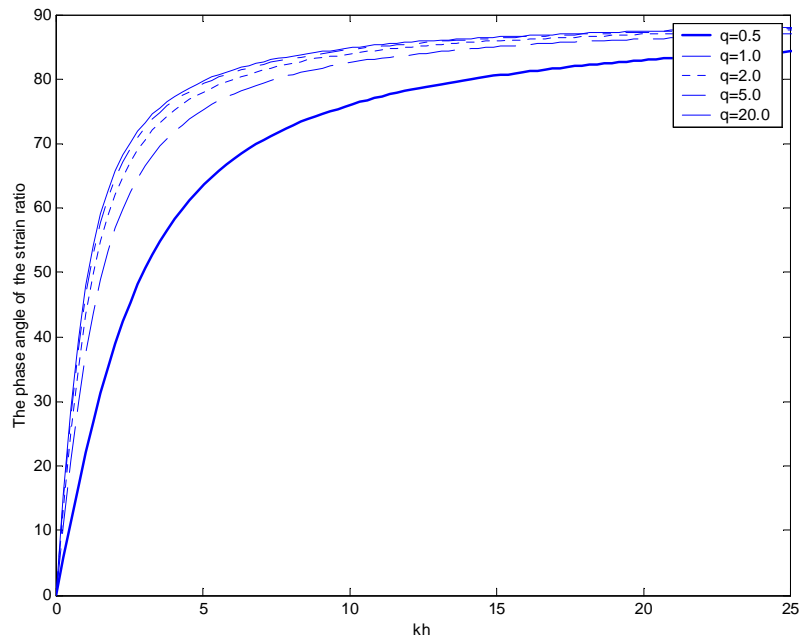
Figure 3.7: Phase angle of κ under different loading frequencies
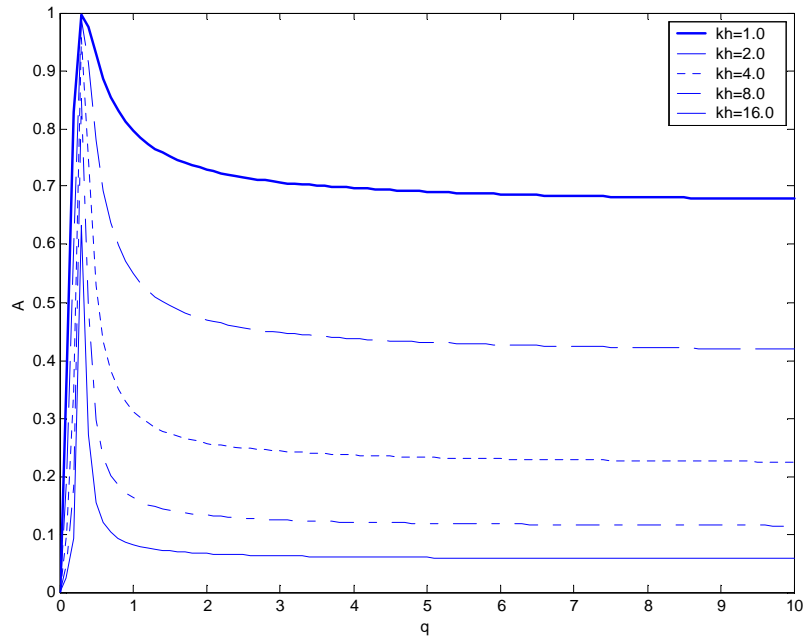
Figure 3.8: Amplitude of κ with different material combinations
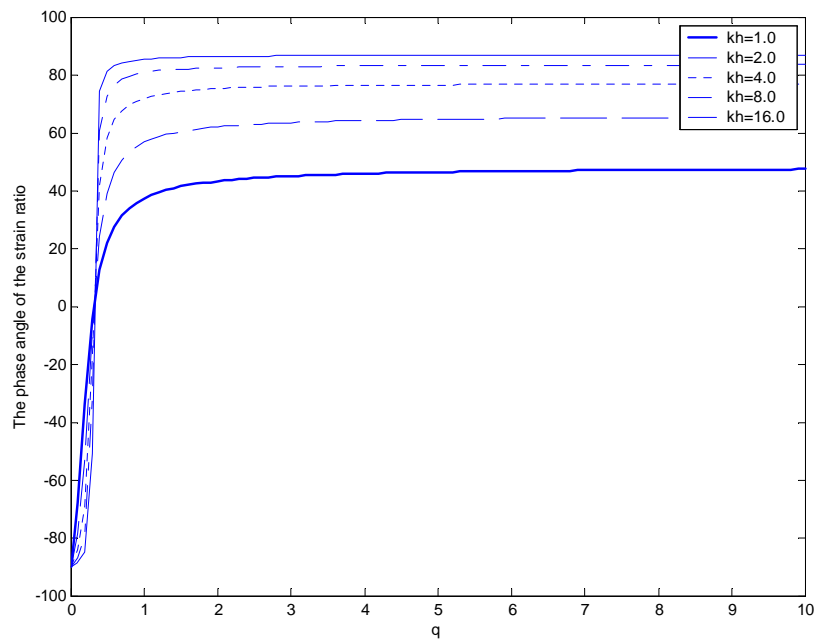
Figure 3.9: Phase angle of κ with different material combinations

3.2.2.2 Interfacial Debonding

If the sensor is not perfectly bonded to the host structure, the interfacial defection will disturb the dynamic load transfer and consequently affect the performance of the piezoelectric sensor. The dynamic strain ratio will be dependent on the location along the interface, which can be expressed by using Equation (3.43) and (3.17):

$$\kappa(\tilde{y}) = \kappa + \frac{\sum_{j=1}^{N} C_j h_j(\tilde{y})}{\tilde{\varepsilon}_y^I} \qquad (3.50)$$

where κ is given by Equation (3.48), representing the strain ratio of the perfect bonding case. C_j are the coefficients of Chebyshev polynomials in Equation (3.36), $\tilde{\varepsilon}_y^I$ and $h_j(\tilde{y})$ are given by Equation (3.42) and Equation (3.44), respectively.

For the static case where $k = k_0 = k_s = 0$, the right hand side of Equation (3.41) equals zero, so the coefficients C_j are zero as well, and κ in Equation (3.50) becomes 1. Therefore, the strain ratio $\kappa(\tilde{y})$ given by (3.50) becomes a constant value $\kappa(\tilde{y}) = \kappa = 1$.

3.2.2.3 The Effect of the Loading Frequency

The loading frequency will have significant effects upon the load transfer between the sensor and the host structure. Three cases are considered with $q = 0.5$, $\upsilon = 5.0$; $q = 5.0$, $\upsilon = 5.0$; and $q = 0.5$, $\upsilon = 20.0$, which is given by Equation (3.46) and (3.47). A series of the loading frequency (kc) values from $kc = 0.0$ to 8.0 are chosen to investigate the effect of different loading frequencies upon the strain distribution.

Figure 3.10 shows the amplitude A of the dynamic strain ratio $\kappa(\tilde{y})$ under relatively low loading frequencies $kc = 0.0, 0.4, 0.8, 1.2$ and 2.0, with $q = 0.5$, $\upsilon = 5.0$. Figure 3.11 shows the amplitude A of the dynamic strain ratio under relatively high loading frequencies $kc = 0.0, 2.0, 4.0$ and 8.0, with $q = 0.5$, $\upsilon =$

5.0. Figure 3.12 shows the amplitude A of $\kappa(\tilde{y})$ for a relatively soft sensor with $q = 5.0$, $\upsilon = 5.0$. For a more detailed look, Figure 3.13 and Figure 3.14 show the amplitude A and the phase angle θ of the dynamic strain ratio $\kappa(\tilde{y})$ when $q = 0.5$ and $\upsilon = 20.0$.

From the results it can be observed that the loading frequency has much more significant effects upon both the amplitude and the phase angle of the dynamic strain ratio, compared with the results of the perfect-bonding situation. As shown in Figure 3.10, when $kc = 0$, which corresponds to the static case, the value of the strain ratio is constantly equal to 1. When the loading frequency increases, the amplitude of the dynamic strain ratio increases, with the maximum and minimum values of the amplitude around the crack tips $y/c = \pm 1$. In Figure 3.11, as the loading frequency continues to increase from 2.0 to 8.0, the magnitude of A increases significantly. In the area away from the crack, the number of peaks increases, as the loading frequency gets higher. For a soft sensor $q = 5.0$ in Figure 3.12, the amplitude curve becomes very complicated when the loading frequency reaches $kc = 2.0$. For a stiff and thin sensor as shown in Figure 3.13, the suitable loading frequency may be $kc \leq 2.0$. The phase angle of the dynamic strain ratio curve shows significant dependence on the loading frequency as well. As shown in Figure 3.13, for the static case, $kc = 0$, the dynamic strain ratio is constantly 1, which corresponds to a constant phase angle of 0. When the loading frequency is relatively low, for $kc = 1.0$ or 2.0, the curve is smooth, and the maximum and minimum value of the phase angle occur around the crack tips. When the loading frequency continues to increase, more peaks appear and the difference of the phase angle as large as $360°$ can be observed in Figure 3.14. However, compared with the low frequency loading condition, the location where the greatest change of the phase angle is further away from the crack tips.
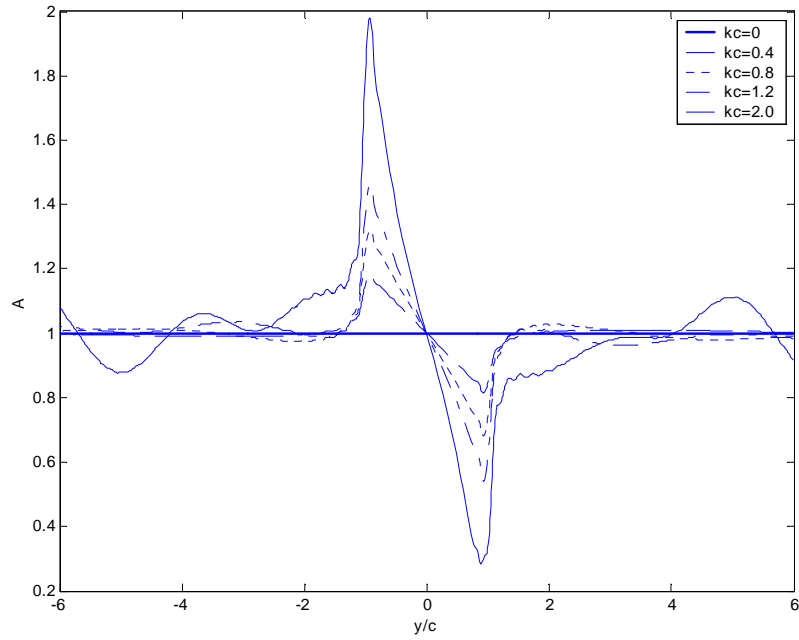
Figure 3.10: Amplitude of $\kappa(y)$ with relatively low kc ($q = 0.5$, $\upsilon = 5.0$)
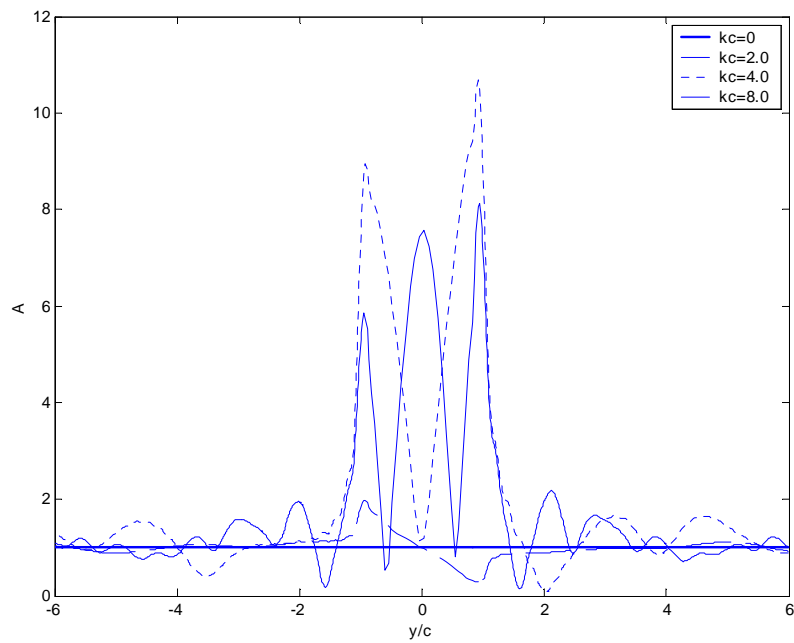
Figure 3.11: Amplitude of $\kappa(y)$ with high kc ($q = 0.5$, $\upsilon = 5.0$)
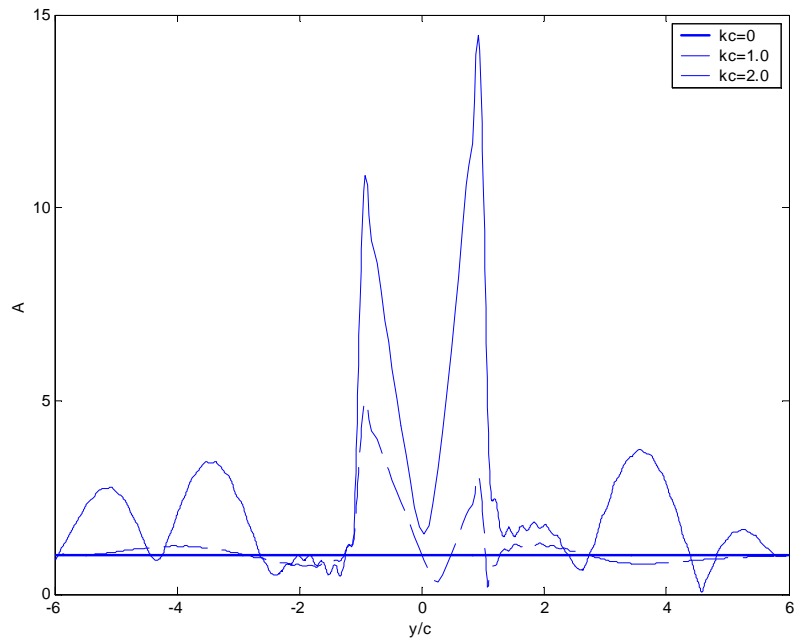
Figure 3.12: Amplitude of $\kappa(y)$ with different kc ($q = 5.0$, $\upsilon = 5.0$)
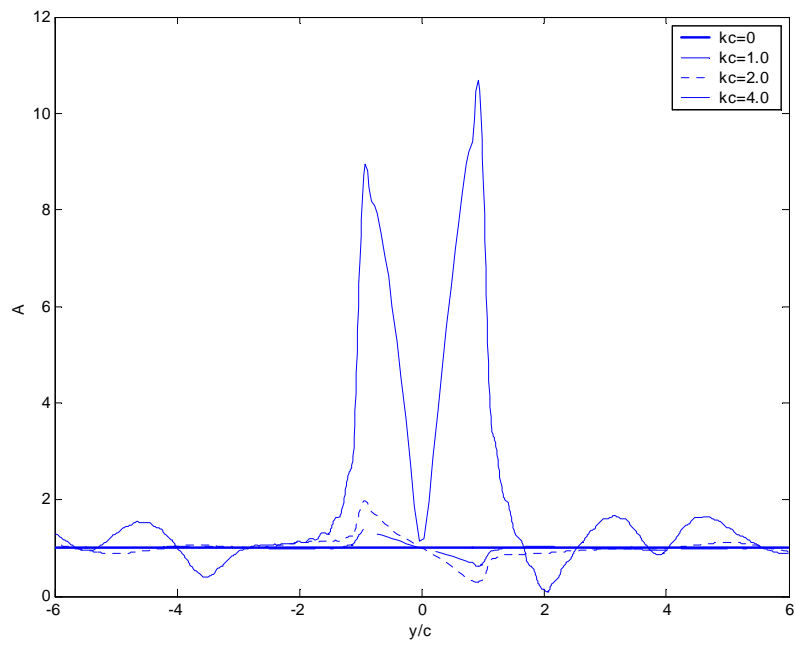
Figure 3.13: Amplitude of $\kappa(y)$ under different kc ($q = 0.5$, $\upsilon = 20.0$)
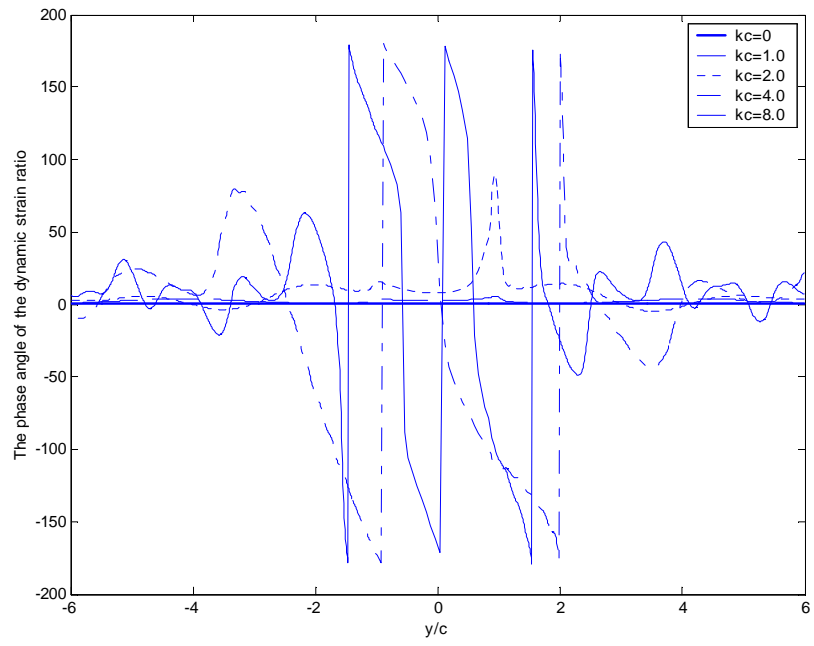
Figure 3.14: Phase angle of $\kappa(y)$ under different kc ($q = 0.5$, $\upsilon = 20.0$)

3.2.2.4 The Effect of the Material Combination

Compared with the perfect-bonding situation, the material mismatch factor q has more significant effect upon the load transfer between the imperfectly bonded sensor and the host medium. Typical examples are shown in Figure 3.15 and Figure 3.16.

Figure 3.15 shows the effect of the material mismatch upon the amplitude of the dynamic strain ratio for the case where $kc = 1.0$, $\upsilon = 5.0$. For a relatively stiff sensor with a low material combination $q = 0.1$, the curve is flat and the value of the amplitude is around 0.8, which is close to the analytical solution of the dynamic strain ratio κ of perfect-bonding situation. It means that when the sensor is very stiff, the disturbance of interfacial debonding becomes insignificant to the dynamic load transfer.

With the decrease of the stiffness of the sensor, the disturbance of the interfacial crack becomes more important. When the material combination q reaches 5.0, the maximum value of the dynamic strain ratio at the crack tips can reach about 5.0. Considering the fact that higher q value corresponding to softer sensor, the current result indicates that, even when the host medium is much stiffer than the sensor, the effect of the interfacial crack upon the load transfer will still be very important.

The change of the dynamic load transfer becomes more complicated for higher loading frequency case. From Figure 3.16 we can see that the number of the peaks increases with the increase of q, but the peak value of the amplitude will rise to a maximum value when q reaches 2.0 and decrease when q continues to increase.
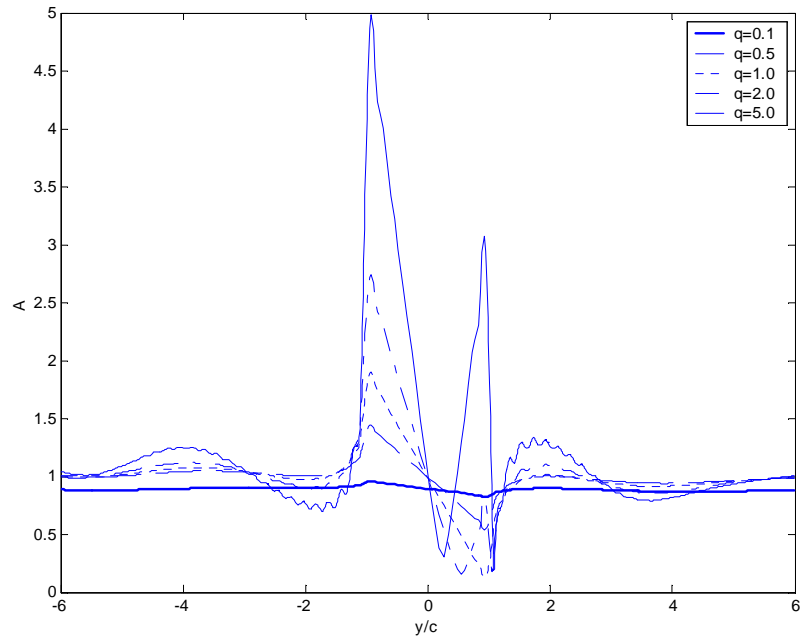
Figure 3.15: Amplitude of $\kappa(y)$ with different q ($kc = 1$, $\upsilon = 5.0$)
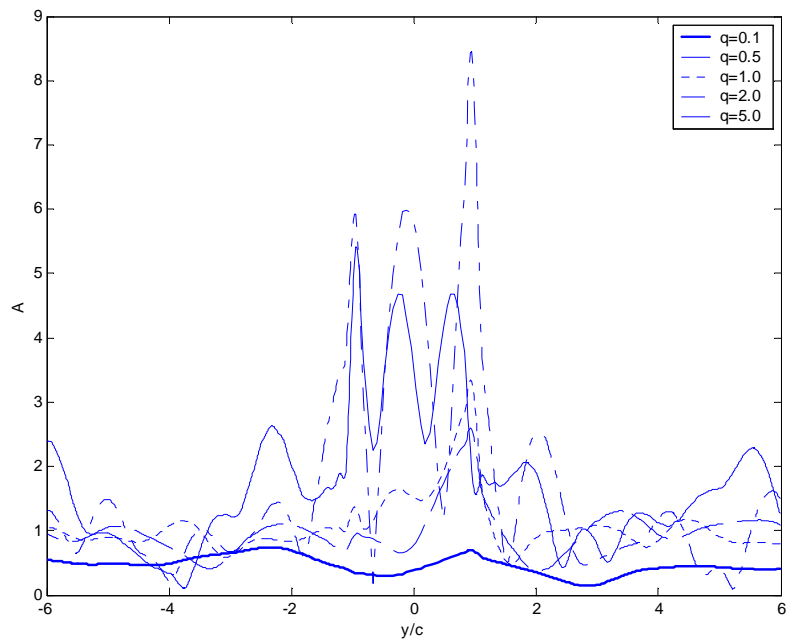
Figure 3.16: Amplitude of $\kappa(y)$ with different q ($kc = 4$, $\upsilon = 5.0$)

3.2.2.5 The Effect of the Geometry of the Sensor

As the results shown above, the ratio of the length of the interfacial debonding to the thickness of the sensor, denoted by υ, will also affect the load transfer between the sensor and the host medium. For the sake of convenience, the crack length c is set as constant, and the thickness of the sensor h varies, corresponding to different values of the geometry ratio υ defined by Equation (3.46). The result is shown in Figure 3.17, with the loading frequency $kc = 1.0$ and the material combination factor $q = 0.5$. With the increase of the value of υ from 5.0 to 100.0, the value of the dynamic strain ratio in the vicinity of the crack tips drops down from around 1.45 to 1.25, which means the disturbance of the interfacial crack becomes more and more insignificant with the decrease of the thickness of the sensor. Compared with the result of the perfectly bonded situation, the influence of interfacial crack upon the dynamic load transfer can be clearly seen. Even for a relatively small-sized crack or a relatively thick sensor, $\upsilon = 5.0$ for example, the amplitude of κ for perfectly bonded case is about 0.98, while the maximum value of the amplitude for the interfacial-debonding situation is as large as 1.45 in Figure 3.17.

3.2.3 Output Voltage

Since the sensor operates in an open-loop mode with no external charges applied to it [83], therefore, the electric displacement across the sensor will be zero, that is,

$$D_z = 0 . \qquad (3.51)$$

Then the electric field intensity, E_z, defined in Equation (3.6), can be expressed as follow:

$$E_z = -\frac{e_s}{\lambda_s}\frac{\partial u_y^s}{\partial y} \qquad (3.52)$$

According to the relationship between voltage and electric field intensity, the voltage distribution along the sensor can be expressed in terms of the axial strain ε_y^s as follow:

$$V(y) = -\int_0^h E_z(y)dz = \frac{e_s h}{\lambda_s}\frac{\partial u_y^s}{\partial y} = \frac{e_s h}{\lambda_s}\varepsilon_y^s \qquad (3.53)$$

where ε_y^s can be obtained using Equation (3.43), with e_s, λ_s being the effective piezoelectric material constants of the sensor given by Equation (3.8).

Figure 3.18 shows the result of the distribution of voltage along the interface between a typical piezoelectric sensor (PZT-4) and the host medium under loading frequency $kc = 2.0$ with $q = 0.54$, $\upsilon = 20.0$, for both the perfect bonding and imperfect bonding conditions. We can observe that with interfacial debonding the output voltage varies significantly along the interface, and around the tips of the interfacial debonding $y/c = \pm 1$, the voltage measured by the sensor can be increased by about 1.5 times. Here the voltage has been normalized by $\overline{V} = V/V^*$, with $V^* = \frac{e_s h}{\lambda_s}\varepsilon_y^I$.

Since the output voltage is an important indication of the characteristics of the sensor system, we consider the effects of the mentioned parameters upon V_{max}, the maximum value of the voltage along the longitudinal axis inside the sensor, and V_{max} is normalized by $\overline{V}_{max} = V_{max}/V^*$ as well.

The $\overline{V}_{max} - kc$ curves in Figure 3.19 and Figure 3.20 show the significant effect of υ upon the maximum output voltage for both relatively stiff and soft sensors. The number and the value of peaks in the curves increase with the increase of υ. For a softer sensor with $q = 5.0$, this effect is much more significant and the peak values of the amplitude of $\overline{V}_{max}$ correspond to lower loading frequencies.

Moreover, since υ represents the relative thickness of the sensor, if υ is too small, many other factors will affect the physical phenomena of the problem and the one-dimension sensor model may not be suitable for use. Therefore, we don't consider the situations when $\upsilon < 5.0$.
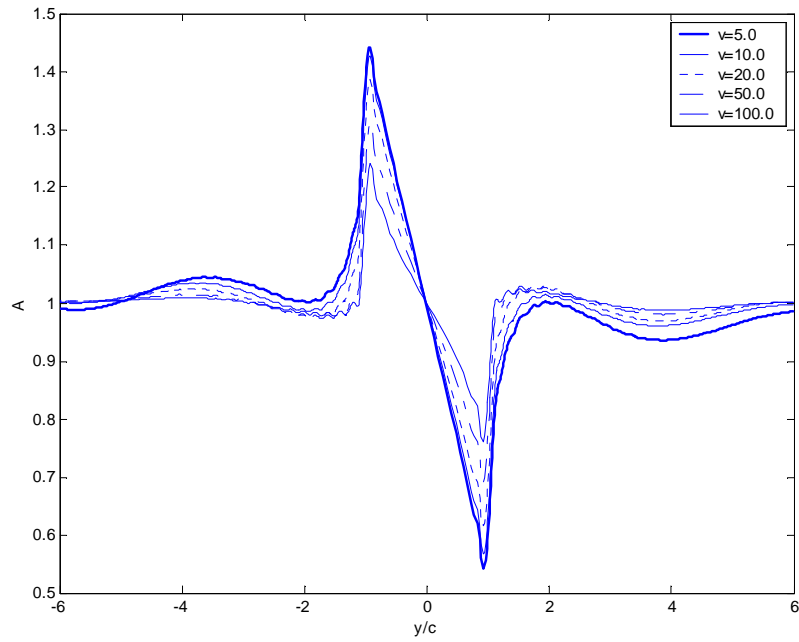
Figure 3.17: Amplitude of $\kappa(\tilde{y})$ with different geometries ($kc = 1.0$, $q = 0.5$)
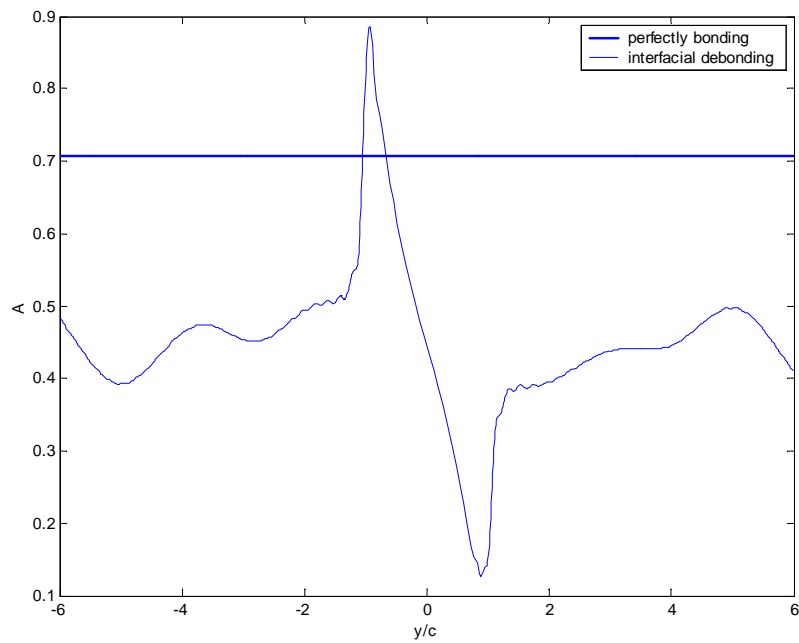
Figure 3.18: The distribution of $\overline{V}$ ($kc = 2.0$, $q = 0.5$, $\upsilon = 20.0$)
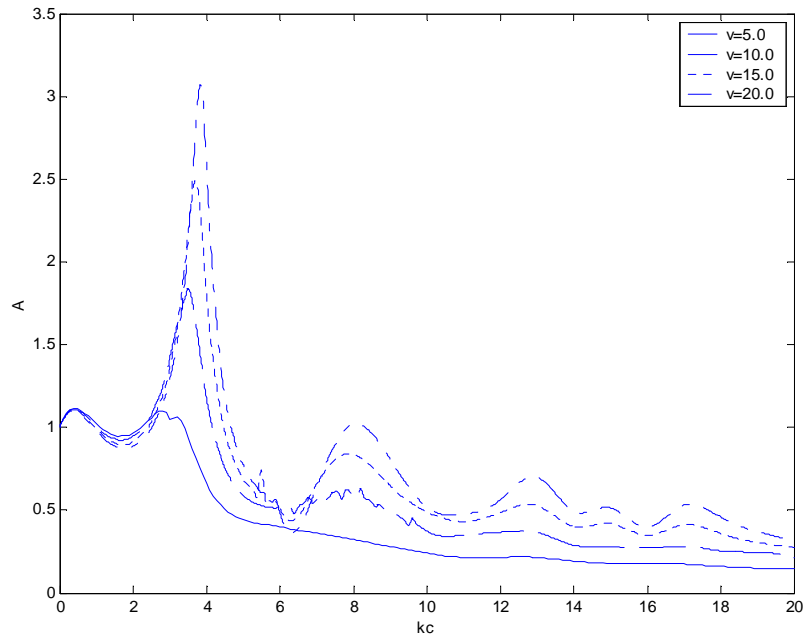
Figure 3.19: Amplitude of $\overline{V}_{\max}$ under different loading frequencies ($q = 0.5$)
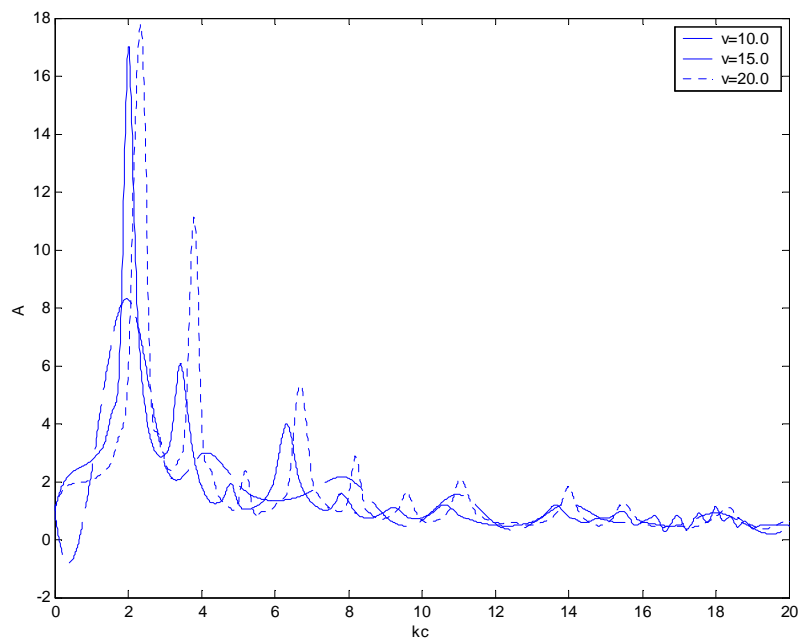
Figure 3.20: Amplitude of $\overline{V}_{\max}$ under different loading frequencies ($q = 5.0$)

3.3 Concluding Remarks

Numerical simulation is conducted to describe the coupled dynamic behavior of a surface bonded sensor attached to an elastic host medium. When the system is subjected to high frequency mechanical loads, the effects of loading frequency, material combination and sensor geometry upon the load transfer have been studied, and comparison between a perfect-bonding sensor system and an imperfect-bonding sensor system has been performed. The analysis is based on the use of the integral transform method and the solution of singular integral equations using Chebyshev polynomials. The results reveal the dependence of the dynamic strain ratio and the maximum output voltage of the sensor upon the mentioned factors, and specific conclusions are obtained from the results of typical examples:

(1). For the perfectly bonded sensor system, when a plane harmonic wave is applied, the load transfer is constant along the interface between the sensor and the host structure, and the effect of loading frequency upon the dynamic strain ratio is insignificant. The material combination will affect the sensing ability, and there is a critical value of the material mismatch factor q, depending on the incident angle of the incident wave as mechanical loads, as well as Poisson's ratio v. The amplitude of the dynamic strain ratio will increase with q when $q < q^c$, and then decrease with the increase of q when $q > q^c$. This proves that the current perfect bonded sensor system is reliable for high frequency applications, with material combinations properly chosen.

(2). The loading frequency plays a much more important role in the imperfect bonding sensor system. Based on the current simulation, relatively low frequencies $kc \leq 2.0$ are more suitable for the detection of debonding with the predictable results. Moreover, the peaks of the dynamic strain ratio appear in the vicinity of the interfacial debonding with larger amplitudes, which increase with the increase of the loading frequency. With respect to higher frequencies, $kc > 4.0$ for example, the maximum voltage detected by the sensor varies significantly and becomes very complicated with the change of

loading frequency. This means that the interfacial debonding will decrease the sensing ability of the current sensor system significantly especially under high frequency conditions.

(3). The material combination q and the sensor geometry υ show more significant influence on the dynamic load transfer when the sensor is not perfectly bonded. Under low loading frequencies, q from 0.5 to 5.0, and υ from 5.0 to 20.0 might be more suitable for detecting incident waves, showing less significant disturbance from the interfacial debonding.

§4 Wave Propagation in the Piezoelectric Sensor System

This chapter provides an analytical and numerical study to simulate the surface wave propagation in an elastic half plane that is surface-bonded to a surface bonded piezoelectric sensor system under high-frequency mechanical loads. This solution is based on the developed one-dimensional sensor model, and the resulting wave propagation is determined by using integral transform method and solving the resulting integral equations. The work is concerned with the behavior of the interface waveform and far field waveform generated by the surface-bonded sensor with interfacial debonding.

4.1 Waveforms in Perfectly Bonded Sensor System

When the piezoelectric sensor is perfectly bonded, a dynamic displacement wave will be generated inside the host medium with an incident wave applied to the host medium. For a sensor system subjected to a high-frequency harmonic wave as the mechanical load, by substituting Equation (3.28) into (3.26), and applying the inverse Fourier transform, the waveform can be obtained:

$$u_y^{\tau} = u_y^I \frac{\beta \left[2s^2 e^{\alpha z} - (2s^2 - k^2)e^{\beta z} \right]}{m(s)} \Bigg|_{s=k_0} \qquad (4.1)$$

By substituting Equation (3.28) into (3.26), and by applying inverse Fourier transform, the corresponding components of the stress wave field can be written as:

$$\sigma_y^s(y,z) = -\varepsilon_y^I \cdot H_1(k_0, z)$$
$$\sigma_z^s(y,z) = -\varepsilon_y^I \cdot H_2(k_0, z) \qquad (4.2)$$
$$\tau_{yz}^s(y,z) = -\varepsilon_y^I \cdot H_3(k_0, z)$$

where

$$H_1(s,z) = -\frac{2\beta}{m(s)\cdot\Delta}\left[-\left(k^2+2\alpha^2\right)e^{\alpha z}+(2s^2-k^2)e^{\beta z}\right]$$

$$H_2(s,z) = -\frac{2\beta}{m(s)\cdot\Delta}\left(2s^2-k^2\right)\left[e^{\alpha z}-e^{\beta z}\right] \tag{4.3}$$

$$H_3(s,z) = -\frac{1}{s\cdot m(s)\cdot\Delta}\left[4s^2\alpha\beta e^{\alpha z}-(2s^2-k^2)^2 e^{\beta z}\right]$$

with u_y^I and ε_y^I are given by Equation (3.17).

From Expression (4.1)-(4.3) we can see that the induced wave field is still a plane harmonic wave, with the amplitude reducing with the distance from the sensor.

4.2 Wave Propagation in Imperfectly Bonded Sensor System

For an imperfectly boned sensor system, not only the sensor, but also the interfacial delamination, will affect the wave field inside the host medium. By applying inverse Fourier Transform to Equations (3.26), and by using Equation (3.32), the general solutions of the induced wave can be obtained as

$$\sigma_y(y,z) = \sigma_y^s(y,z)+\sigma_y^d(y,z)$$
$$\sigma_z(y,z) = \sigma_z^s(y,z)+\sigma_z^d(y,z) \tag{4.4}$$
$$\tau_{yz}(y,z) = \tau_{yz}^s(y,z)+\tau_{yz}^d(y,z)$$

with $\sigma_y^s(y,z), \sigma_z^s(y,z)$ and $\tau_{yz}^s(y,z)$ representing the contribution of the sensor to the induced stress wave field, given by Equation (4.2); and $\sigma_y^d(y,z), \sigma_z^d(y,z)$ and $\tau_{yz}^d(y,z)$ representing the contribution of the interfacial debonding to the induced stress wave field, where

$$\sigma_y^d(y,z) = \sum_{j=1}^{N}C_j\begin{cases}(-1)^n\int_0^\infty H_1(s,z)J_j(sc)\sin(sy)ds & j=2n+1 \\ (-1)^n\int_0^\infty H_1(s,z)J_j(sc)\cos(sy)ds & j=2n\end{cases}$$

$$\sigma_z^d(y,z) = \sum_{j=1}^{N}C_j\begin{cases}(-1)^n\int_0^\infty H_2(s,z)J_j(sc)\sin(sy)ds & j=2n+1 \\ (-1)^n\int_0^\infty H_2(s,z)J_j(sc)\cos(sy)ds & j=2n\end{cases}$$

$$\tau_{yz}^d(y,z) = \sum_{j=1}^{N}C_j\begin{cases}(-1)^n\int_0^\infty H_3(s,z)J_j(sc)\cos(sy)ds & j=2n+1 \\ (-1)^{n+1}\int_0^\infty H_3(s,z)J_j(sc)\sin(sy)ds & j=2n\end{cases}$$

4.2.1 Far Field Wave Field

With the solved coefficients of Chebyshev polynomials given by Equation (3.36), the stress wave field can be determined. Although the resulting waveform is very complicated ad Equations (4.4), the fundamental behavior of the propagating wave can be predicted from wave field far away from the sensor. For any far field point at the lower half space, its position can be presented in the polar coordinate as

$$y = R\cos\eta, \quad z = -R\sin\eta, \quad 0 < \eta < \pi \tag{4.5}$$

where R denotes the distance from the center of the sensor, η denotes the position angle with respect to y axis. Making use of the relation of

$$e^{isy} = \cos sy + i\sin sy \tag{4.6}$$

The shear stress wave $\tau_{yz}(y,z)$ in the far field brought by the interfacial debonding can be rewritten as

$$\tau_{yz}^f(y,z) = \tau_{yz}^0(y,z) + \sum_{j=1}^{N} C_j \left\{ \int_{-\infty}^{\infty} \frac{N_j^1 J_j(sc)(4s^2\alpha\beta)e^{-R(\alpha\sin\eta - is\cos\eta)}}{s \cdot m(s) \cdot \Delta} ds \right.$$
$$\left. - \int_{-\infty}^{\infty} \frac{N_j^1 J_j(sc)(2s^2 - k^2)^2 e^{-R(\beta\sin\eta - is\cos\eta)}}{s \cdot m(s) \cdot \Delta} ds \right\} \tag{4.7}$$

where $\tau_{yz}^0(y,z)$ represents the surface wave field along the interface induced by the interfacial debonding between the sensor and the host structure due to the singularity of the above integral, and

$$N_j^1 = \begin{cases} \dfrac{(-1)^n}{2} & j = 2n+1 \\ \dfrac{(-1)^{n+1}}{2i} & j = 2n \end{cases} \tag{4.8}$$

For $R \gg 1$, the interfacial wave $\tau_{yz}^0(y,z)$, which will decay exponentially with the distance from the interface, will be ignored in the far field solution. The existence of the waveform propagating along the interface will be discussed in the next subsection. For Equation (4.7), since the exponential functions $e^{-R(\alpha\sin\eta - is\cos\eta)}$ and $e^{-R(\beta\sin\eta - is\cos\eta)}$ are rapidly changing functions compared with kernel functions in the above obtained integral, the dominant contribution to the

integral comes from the neighborhood of the points $s = s_0$ and $s = s_1$, where $\alpha \sin \eta - is \cos \eta$ and $\beta \sin \eta - is \cos \eta$ are the smallest, respectively. The accuracy of that dominant contribution improves with increasing R. Based on this idea, the method of steepest descent will be used in the following discussion [80], i.e. to deform the path of integration in the s-plane in Equation (4.7) into a contour along the path of steepest descent, which passes through the saddle point(s). The saddle points can be determined by differentiation of $h_0(s) = \alpha \sin \eta - is \cos \eta$ and $h_1(s) = \beta \sin \eta - is \cos \eta$, as $s_0 = K \cos \eta$ and $s_1 = k \cos \eta$, respectively. At the saddle points we subsequently find

$$h_0(s)\big|_{s=s_0} = -Ki, \qquad h_0^{''}(s)\big|_{s=s_0} = \frac{i}{K \sin^2 \eta}$$

$$h_1(s)\big|_{s=s_1} = -ki, \qquad h_1^{''}(s)\big|_{s=s_1} = \frac{i}{k \sin^2 \eta} \qquad (4.9)$$

The direction of the steepest descent path can be determined using

$$\arg\left[\frac{1}{2} h_0^{''}(s)\big|_{s=s_0} e^{2i\theta_{s0}}\right] = 0, \arg\left[\frac{1}{2} h_1^{''}(s)\big|_{s=s_1} e^{2i\theta_{s1}}\right] = 0 \qquad (4.10)$$

with "arg" representing the argument of a complex number. The solutions of (4.10) are $\theta_{s0} = \theta_{s1} = -\dfrac{\pi}{4}$.

Therefore, the approximation of the induced wave in the far field induced by the interfacial crack can be written as

$$\tau_{yz}^f = \sum_{j=1}^{N} C_j N_j^1 \left[f_0(j,\eta)\sqrt{\frac{2\pi K}{R}} e^{i\left(KR-\frac{\pi}{4}\right)} + f_1(j,\eta)\sqrt{\frac{2\pi k}{R}} e^{i\left(kR-\frac{\pi}{4}\right)} \right] \qquad (4.11)$$

where

$$f_0(j,\eta) = \frac{g_0(j,\eta)}{p(\eta)}, f_1(j,\eta) = \frac{g_1(j,\eta)}{q(\eta)}$$

$$g_0(j,\eta) = -4J_j(K\cos\eta)K^2\sin^2\eta\cos\eta\sqrt{k^2 - K^2\cos^2\eta}$$

$$g_1(j,\eta) = -\frac{J_j(k\cos\eta)}{k\cos\eta}\sin\eta\left(2k^2\cos^2\eta - k^2\right)^2$$

$$p(\eta) = i\frac{k^2\sqrt{k^2 - K^2\cos^2\eta}}{\mu} + \frac{\Delta_0}{\overline{E}_s h\left(K^2\cos^2\eta - k_s^2\right)}$$

$$q(\eta) = i\frac{k^3\sin\eta}{\mu} + \frac{\Delta_1}{\overline{E}_s h\left(k^2\cos^2\eta - k_s^2\right)}$$

$$\Delta_0 = \left(2K^2\cos^2\eta - k^2\right)^2 + 4K^3\sin\eta\cos^2\eta\sqrt{k^2 - K^2\cos^2\eta}$$

$$\Delta_1 = \left(2k^2\cos^2\eta - k^2\right)^2 + 4ik^3\sin\eta\cos^2\eta\begin{cases}\sqrt{k^2\cos^2\eta - K^2} & k\cos\eta > K \\ -i\sqrt{K^2 - k^2\cos^2\eta} & k\cos\eta < K\end{cases}$$

$$(4.12)$$

Similarly, the far field solution of stress components σ_y and σ_z can be obtained as

$$\sigma_y^f = \sum_{j=1}^N C_j N_j^2\left[f_2(j,\eta)\sqrt{\frac{2\pi K}{R}}e^{i\left(KR - \frac{\pi}{4}\right)} + f_3(j,\eta)\sqrt{\frac{2\pi k}{R}}e^{i\left(kR - \frac{\pi}{4}\right)}\right] \quad (4.13)$$

$$\sigma_z^f = \sum_{j=1}^N C_j N_j^2\left[f_4(j,\eta)\sqrt{\frac{2\pi K}{R}}e^{i\left(KR - \frac{\pi}{4}\right)} + f_5(j,\eta)\sqrt{\frac{2\pi k}{R}}e^{i\left(kR - \frac{\pi}{4}\right)}\right] \quad (4.14)$$

where

$$N_j^2 = \begin{cases}\dfrac{(-1)^n}{2i} & j = 2n+1 \\ \dfrac{(-1)^n}{2} & j = 2n\end{cases} \quad (4.15)$$

and

$$f_2(j,\eta) = \frac{g_2(j,\eta)}{p(\eta)}, f_3(j,\eta) = \frac{g_3(j,\eta)}{q(\eta)}, f_4(j,\eta) = \frac{g_4(j,\eta)}{p(\eta)}, f_5(j,\eta) = -\frac{g_3(j,\eta)}{q(\eta)}$$

$$g_2(j,\eta) = -2iJ_j(K\cos\eta)\sin\eta\sqrt{k^2 - K^2\cos^2\eta}\left(k^2 - 2K^2\sin^2\eta\right)$$

$$g_3(j,\eta) = -2ikJ_j(k\cos\eta)\sin^2\eta\left(2k^2\cos^2\eta - k^2\right)$$

$$g_4(j,\eta) = -2iJ_j(K\cos\eta)\sin\eta\sqrt{k^2 - K^2\cos^2\eta}\left(2K^2\cos^2\eta - k^2\right)$$

$$(4.16)$$

Therefore, the whole wave field inside the host medium can be obtained by the superposition of the waves induced by the sensor and by the interfacial defection as

$$\sigma_y = \sigma_y^s + \sigma_y^f$$
$$\sigma_z = \sigma_z^s + \sigma_z^f \qquad (4.17)$$
$$\tau_{yz} = \tau_{yz}^s + \tau_{yz}^f$$

4.2.2 Interfacial Wave Propagation

From the previous discussion we have known that along the interface between the sensor and the host medium, an interfacial wave will be generated. This wave shows no decay during propagation for ideal linear elastic medium. To evaluate the behavior of this interfacial wave generated, let us consider the induced shear stress τ_{yz} by the interfacial debonding along the interface,

$$\tau_{yz}(y,0) = \tau_{yz}^s(y,0) + \sum_{j=1}^{N} C_j \begin{cases} (-1)^n \int_0^\infty \dfrac{1}{s \cdot m(s)} J_j(sc)\cos(sy)ds & j = 2n+1 \\ (-1)^{n+1} \int_0^\infty \dfrac{1}{s \cdot m(s)} J_j(sc)\sin(sy)ds & j = 2n \end{cases} \qquad (4.18)$$

Here $\tau_{yz}^s(y,0)$ denotes the contribution of the sensor to the interfacial wave, which can be obtained by using Equation (4.2).

The second part in the right-hand side of Expression (4.18) demonstrates the shear stress wave brought by the interfacial debonding, which is denoted by τ_{yz}^{d0}. When $m(s)$ approaches zero at a special value $s = s_0$, the integral becomes singular when $s = s_0$, where $s_0 = \omega/c_0$, with c_0 being the speed of this interfacial wave. The governing equation for determining s_0 is $m(s) = 0$, which can be rewritten as:

$$\Delta = \frac{\overline{E}_s}{\mu} \frac{k^2 \beta(s^2 - k_s^2)}{\upsilon} \qquad (4.19)$$

where $\Delta(s) = (2s^2 - k^2)^2 - 4s^2\alpha\beta$.

Around the point $s = s_0$, $m(s)$ can be written as

$$m(s) \approx \frac{s - s_0}{g_0}, s \to s_0 \qquad (4.20)$$

with

$$g_0 = \left. \frac{1}{m'(s)} \right|_{s=s_0} \qquad (4.21)$$

This singular term represents the contribution of the interfacial wave.

To evaluate the integration, the contour integration method is used. If the infinite integral of function $f(s)$ exists, it can be expressed as a limit of contour integrals along the contour Γ^0 that goes along the real line from $-a$ to a and then counterclockwise along a semicircle centered at 0 from a to $-a$, as shown in Figure 4.1:

$$\int_{-\infty}^{\infty} f(s)ds = \int_{\Gamma^0} f(s)ds = \int_{\Gamma_0} f(s)ds + \int_{\Gamma_1} f(s)ds + \int_{\Gamma_3} f(s)ds + \int_{\Gamma_4} f(s)ds \quad (4.22)$$

Considering the integration of $f(s)$ along the integration path $\Gamma^1 = \Gamma_0 + \Gamma_2 + \Gamma_3 + \Gamma_4$, the singular point s_0 of $f(s)$ is excluded from the closed integration path, so we can get

$$\oint_{\Gamma} f(s)ds = \int_{\Gamma_0} f(s)ds + \int_{\Gamma_2} f(s)ds + \int_{\Gamma_3} f(s)ds + \int_{\Gamma_4} f(s)ds = 0 \qquad (4.23)$$

By using Jordan's Lemma, $\int_{\Gamma_4} f(s)ds$ becomes zero when the radius a approaches infinity. Equation (4.23) can be written as

$$\int_{\Gamma_0} f(s)ds + \int_{\Gamma_3} f(s)ds = -\int_{\Gamma_2} f(s)ds \qquad (4.24)$$

Substitute Equation (4.24) into Equation (4.22), and use the Residue Theorem, the infinite integral of $f(s)$ can be obtained as

$$\int_{-\infty}^{\infty} f(s)ds = \int_{\Gamma_1} f(s)ds - \int_{\Gamma_2} f(s)ds = 2\pi i \operatorname*{Res}_{s=s_0}[f(s)] \qquad (4.25)$$

Therefore, the part of the resulting interfacial wave caused by the interfacial debonding can be obtained as

$$\tau_{yz}^{d0} = A^{i(s_0 y + \psi)} \qquad (4.26)$$

where

$$A^0 e^{i\psi} = \pi \sum_{j=1}^{N} C_j J_j (s_0 c) \frac{g_0}{s_0} \begin{cases} (-1)^n i & j = 2n+1 \\ (-1)^{n+1} & j = 2n \end{cases} \qquad (4.27)$$

with A^0, ψ being the amplitude and phase angle of the resulting interfacial wave induced by the interfacial debonding, respectively.
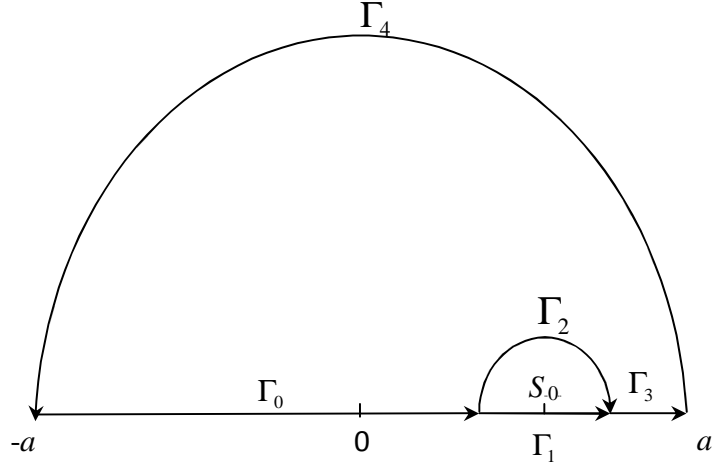
Figure 4.1: The integration path in complex *s* plane

4.3 Results and Discussion

This section will be devoted to the discussion of the behavior of the resulting wave propagation under different geometric and loading conditions. In order to investigate the influence of interfacial debonding upon the induced wave propagation, typical examples are given by both numerical simulation and analytical solutions.

4.3.1 Waves in the Medium

Figure 4.2 and Figure 4.3 show the amplitude of the resulting total elastic wave $\sigma_y^* = \sigma_y / \lambda_0$ and the wave contributed by the interfacial crack $\sigma_y^{d*} = \sigma_y / \lambda_0$, where σ_y^{d*} is given in Equation (4.5), and $\lambda_0 = \mu(1+v)A^I k_0$ with A^I, k_0 being the magnitude and the apparent wave number of the induced wave corresponding to the free-surface boundary condition. The loading frequency is $kc = 3.0$, and other parameters are chosen to be $q = 0.5$, $v = 20.0$ and $\rho_s / \rho_h = 1$. From the figures we can see that along the interface the influence of interfacial debonding on the resulting wave field is significant, and it decreases rapidly with the increase of the distance from the sensor. The interfacial debonding will cause high stress concentration at the tips when $y/c = \pm 1$. Figure 4.4 shows the

amplitude of the resulting total shear stress wave $\tau_{yz}^* = \tau_{yz} / \lambda_0$ with the same loading conditions. Comparing the results in Figure 4.2 and Figure 4.4, we can see that the amplitude of the normal stress is about twice of that of the shear stress, which is believed to be the dominant force to control the interface delamination. The stress component along the z-axis direction σ_z vanishes along the interface, but the stress concentration still appears at the tips of the debonding in the vicinity of the interface, as shown in Figure 4.5. It is small compared with the other two components and can be ignored. The interruption of the interfacial debonding mainly exists in the area of $-4 < z/c < 0$. Figure 4.6 shows the part of the resulting wave contributed by the interfacial debonding, $\sigma_z^{d*} = \sigma_z^d / \lambda_0$.
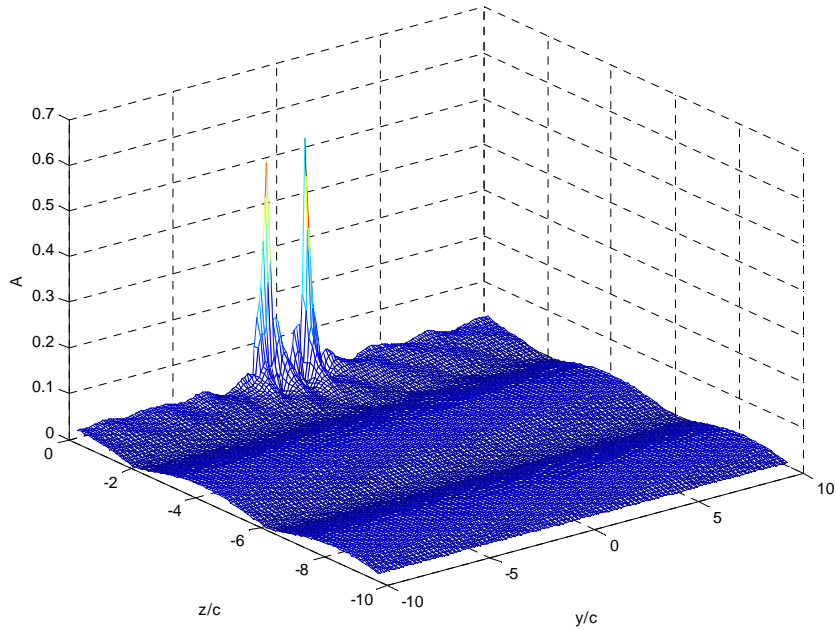
Figure 4.2: The amplitude of σ_y^* $(kc = 3.0, q = 0.5, \upsilon = 20.0)$
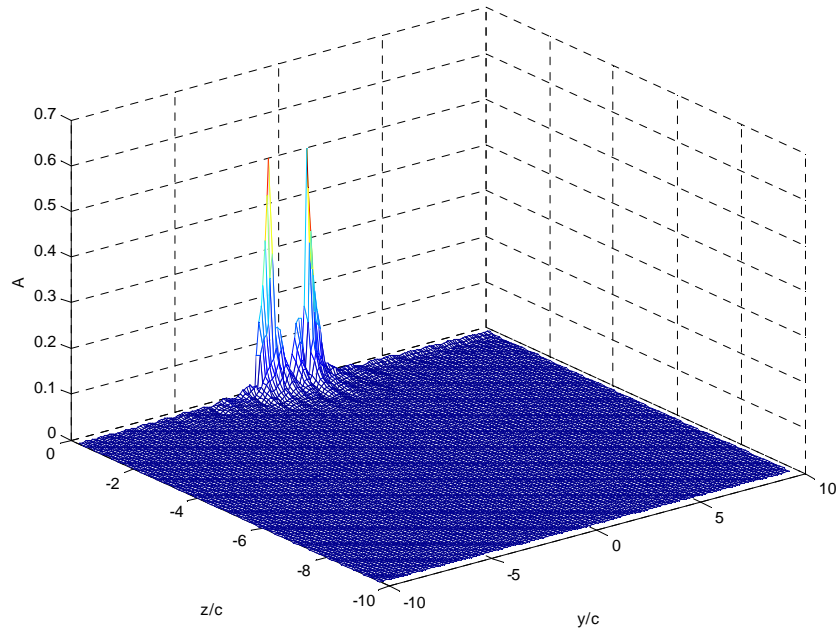
Figure 4.3: The amplitude of σ_y^{d*} ($kc = 3.0, q = 0.5, \upsilon = 20.0$)
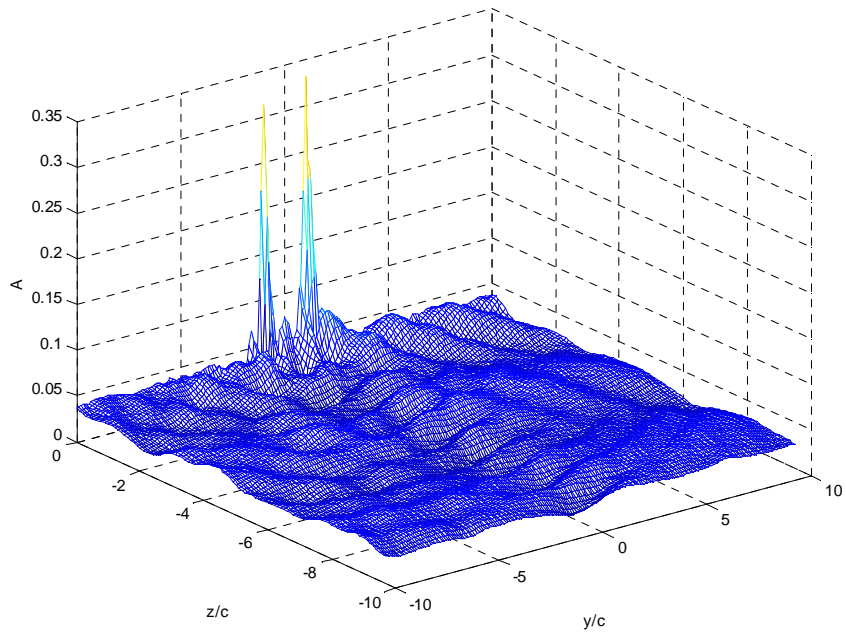
Figure 4.4: The amplitude of τ_{yz}^{*} ($kc = 3.0, q = 0.5, \upsilon = 20.0$)
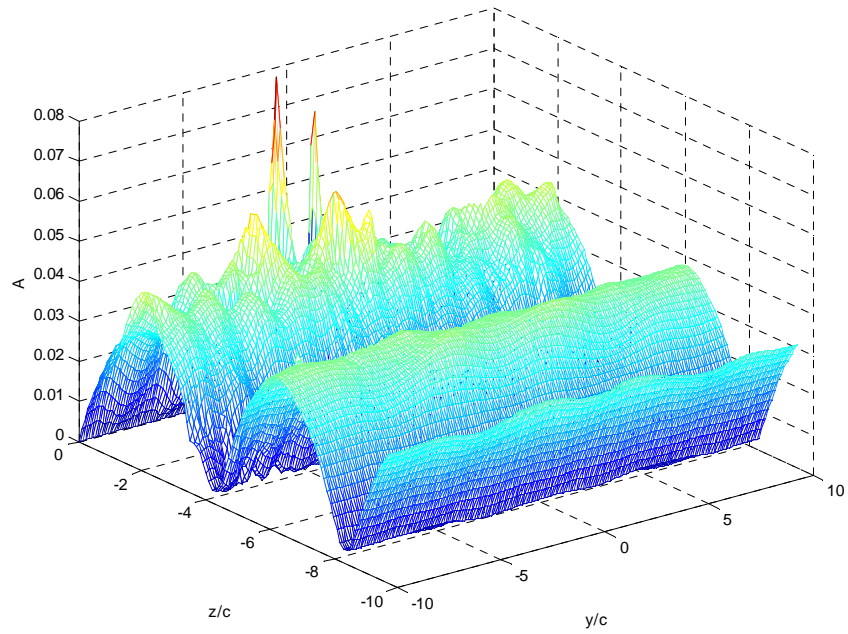
Figure 4.5: The amplitude of σ_z^* $(kc = 3.0, q = 0.5, \ \nu = 20.0)$
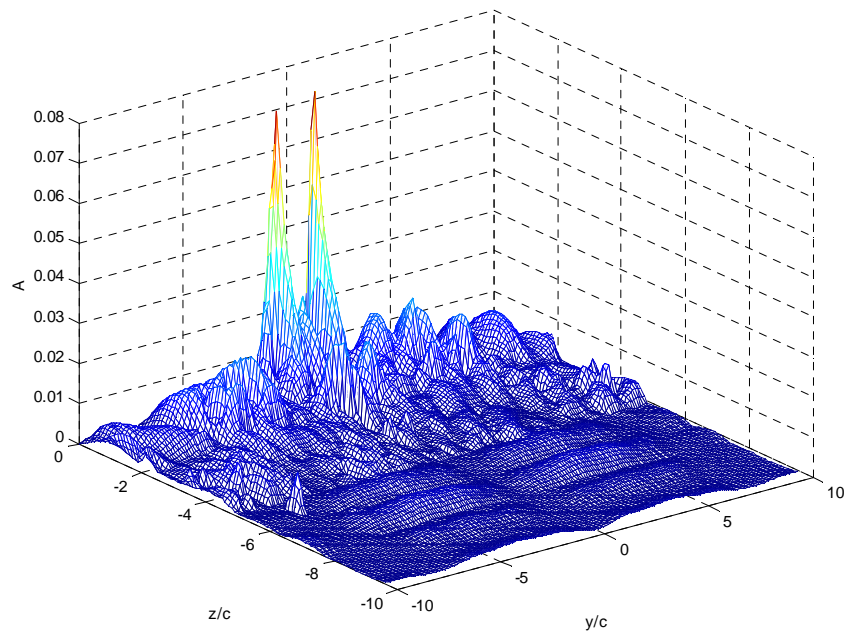
Figure 4.6: The amplitude of σ_z^{d*} $(kc = 3.0, q = 0.5, \ \nu = 20.0)$

4.3.2 Interfacial Waveform

Along the interface between the sensor and the medium $z = 0$, a surface wave with the speed of $c_0 = \omega / s_0$ will be generated, which propagates with non-vanishing amplitude along the surface of the matrix.

The resulting surface wave along the interface between the sensor and the host medium is characterized by Equations (4.20) and (4.21). Figure 4.7 shows the *A-kc* curve of the resulting surface wave corresponding to the contribution from the debonding, which is normalized by $\tau_{yz}^{d0*} = \tau_{yz}^{d0} / \lambda_0$, under different loading frequencies, where a series of material combination factors are chosen as $q = 0.5$, 1.0, 2.0 and 5.0, with $\upsilon = 20.0$. The amplitude of the surface wave increases with the increase of loading frequency *kc*, and the changes are more significant for stiffer sensors ($q = 0.5$ for example). This implies that with the decrease of the stiffness of the sensor, the surface wave will be less significant.
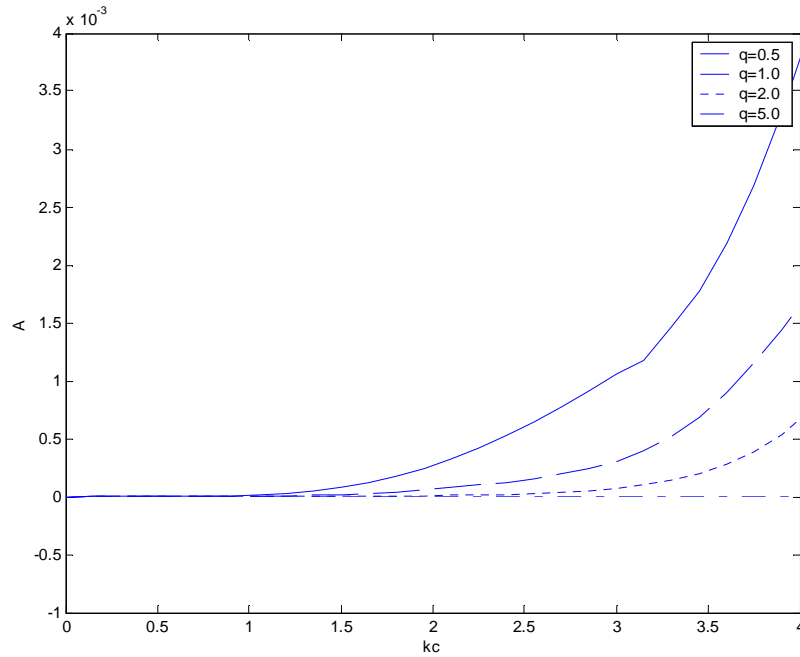
Figure 4.7: The amplitude of τ_{yz}^{d0*} ($\upsilon = 20.0$)

4.3.3 Far Field Waveform

Figure 4.8 compares the normalized far field stress distribution due to debonding $\sigma_z^{f*} = \sigma_z^f / \lambda_0$ at $y/c = 1$, 5 and 10, with that from the asymptotic results, given by Equations (4.4) and (4.14). The loading frequency is $kc = 3.0$ and other parameters are $q = 0.5$, $\upsilon = 20.0$ and $\rho_s / \rho_h = 1$. Very good match between the two curves in Figure 4.8 assures the feasibility of using asymptotic method to simulate the far field stress distribution.

Figure 4.9 , Figure 4.10 and Figure 4.11 give the far field stress distribution σ_z^{f*} using the asymptotic results under the loading frequency $kc = 1.0$, 2.0 and 4.0, respectively. The results show that the maximum value of σ_z^{f*} appears along a straight line when y/c changes from about 20 to 40, corresponding to z/c from -40 to -60. It means that the energy of the far field wave is mainly along the direction $\theta \approx \arctan\left(\dfrac{y_2 - y_1}{z_2 - z_1}\right) = \arctan\left[\dfrac{40 - 20}{(-40) - (-60)}\right] = -45°$, which agrees the results obtained in Equation (4.10). The direction of the main energy of far field is not sensitive to the change of the loading frequency kc, which shows the basic property of the wave propagation in the sensor system with the current mechanical load conditions.
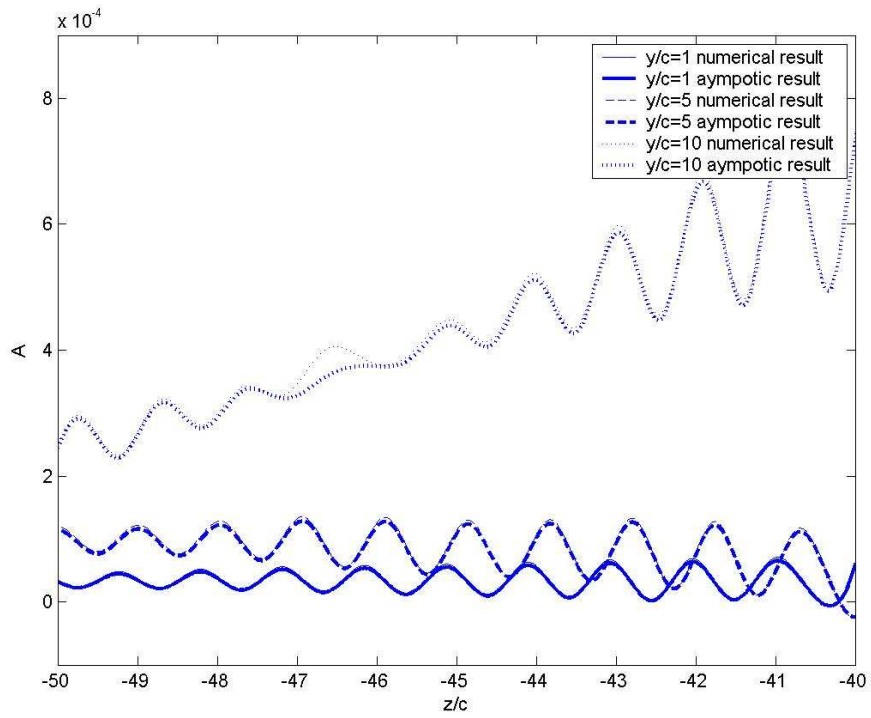
Figure 4.8: The comparison of the far field stress σ_z^{f*}
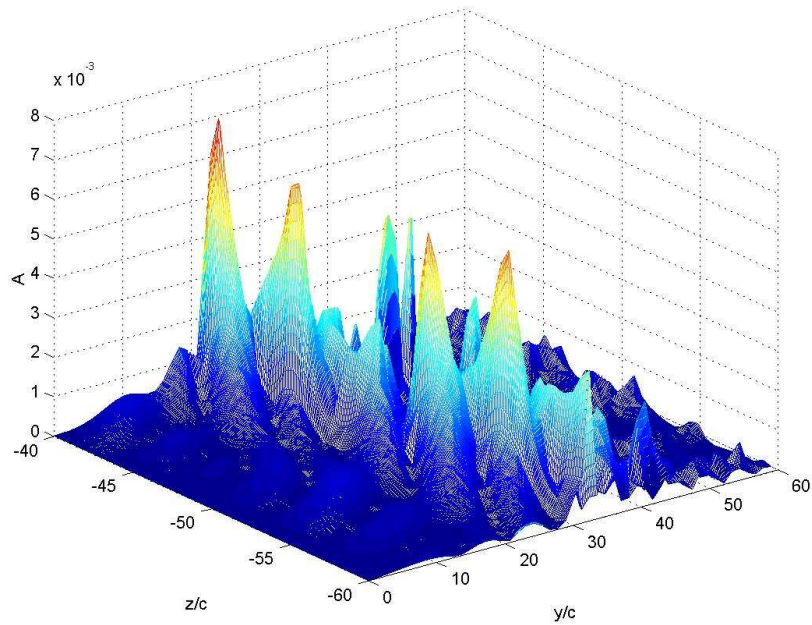
Figure 4.9: The far field stress σ_z^{f*} $(kc = 1.0)$
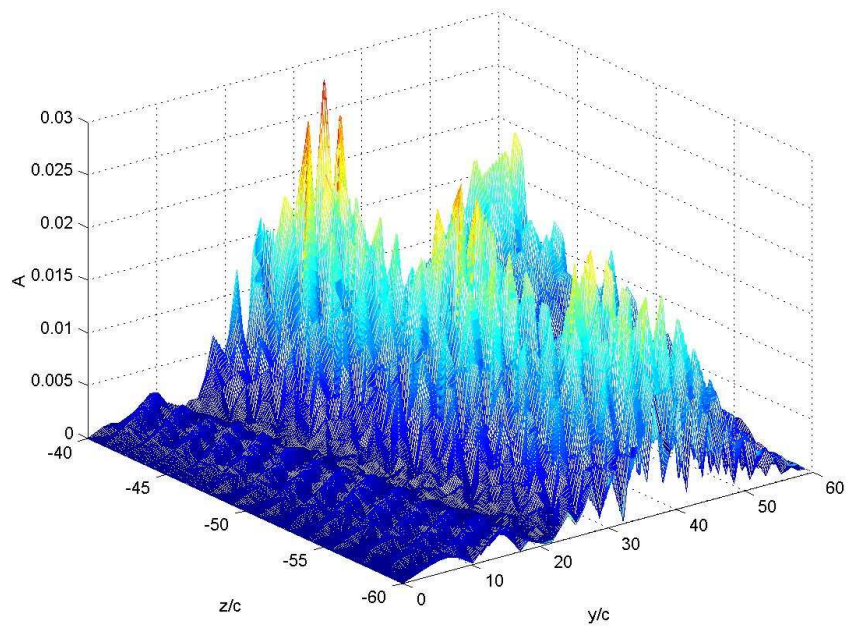
Figure 4.10: The far field stress σ_z^{f*} $(kc = 2.0)$
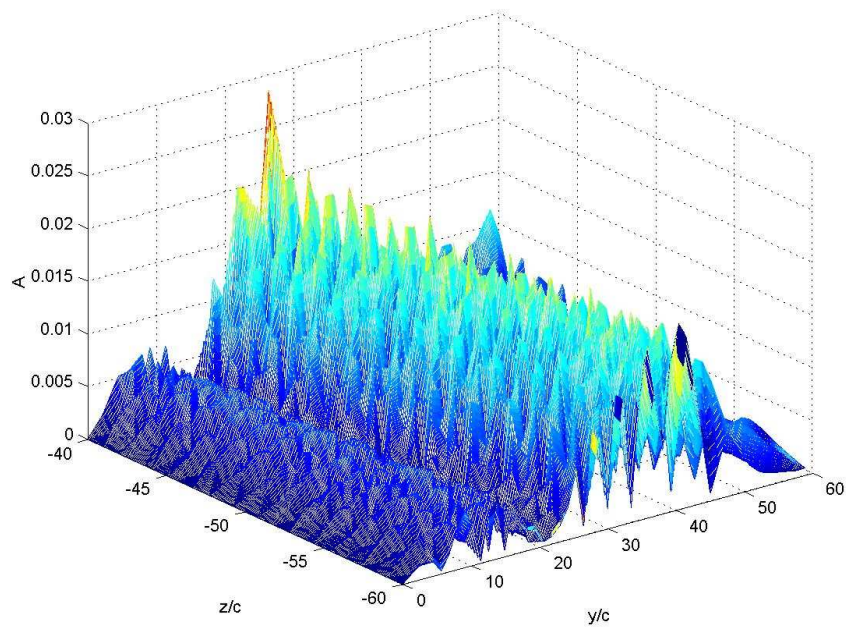
Figure 4.11: The far field stress σ_z^{f*} $(kc = 4.0)$

4.4 Concluding Remarks

The focus of this chapter is on the study of the effect of the wave propagation inside the host medium with an imperfectly bonded piezoelectric sensor, when the system is under high frequency mechanical loads. The high frequency discussed in this chapter corresponds to a wave length of the induced elastic wave comparable to the size of debonding. Typical examples are given for the case when the loading frequencies from $kc = 1.0$ to $kc = 4.0$ and typical material combinations from $q = 0.5$ to $q = 5.0$. The sensor geometry υ is considered as 20.0. Numerical simulation is conducted to investigate the wave propagation inside the host medium and along the interface. For the far field wave propagation, both numerical and asymptotic results are given and compared with each other. Special conclusions are obtained as follows:

(1). For a perfectly bonded sensor system subjected to a high-frequency incident harmonic wave as the mechanical load, the outgoing wave will still be a harmonic wave, and the waveforms can be analytically obtained.

(2). For an imperfectly bonded sensor system, the interfacial debonding will have significant influence upon the induced wave propagation. With the increase of the distance from the sensor, the magnitude of the waves inside the host medium decreases rapidly and the interruption of the interfacial debonding upon the induced waves become more insignificant in the far field.

(3). Along the sensor the dominant stress is the normal stress σ_y^*, which is much higher than the other stress components. In the current results of examples, σ_y^* can be more than twice of the shear stress along the interface. Under high loading frequency situation, combined with the interfacial shear stress, it may lead to the growing of the interfacial debonding and eventually the damage of the surface-bonded sensor system.

(4). For far field wave propagation, the main energy will propagate along z direction and the focus range of the wave energy is not sensitive to the change of the loading frequency, which shows the basic properties of generated wave propagation by surface bonded sensor with the current mechanical loads.

§5 Conclusions and Future Work

5.1 Conclusions

Throughout this study, two major issues essential to the establishment of a structural health monitoring system using surface-bonded piezoelectric sensors are studied:

(1). An one dimensional sensor model has been used to simulate the mechanical and electrical field in a half infinite elastic media due to surface bonded piezoelectric sensor;

(2). The wave propagation induced by piezoelectric sensors is systematically studied through numerical simulation and asymptotic calculation.

Specific contributions and conclusions of this study to the field of the research can be summarized as follows:

(a). The one-dimensional sensor model is used to consider the coupled eletromechanical behavior of a piezoelectric sensor bonded to an infinite elastic medium under plane mechanical loading. Numerical simulations are conducted under different loading frequencies, material combinations and sensor geometries to investigate the dynamic load transfer between the sensor and the host structures, and comparison between the perfect and imperfect bonding conditions are performed.

(b). The simulation results indicate that the loading frequency has much more significant effect upon the load transfer for imperfectly bonding situations other than the perfect bonding condition. Material properties and sensor geometries are more important in imperfect bonding cases, especially under high loading frequency loads. This indicates that the sensing ability of the piezoelectric testing systems are reduced and limited by the interfacial defection greatly, and more careful considerations of the loading conditions as well as the material characteristics are needed.

(c). The wave propagation induced by the surface bonded piezoelectric sensor is analytically studied. The numerical simulation conducted indicates that the

effect of the interfacial defection upon the resulting wave propagation is very significant, especially for high loading frequency cases. The basic properties of the wave field are demonstrated by the analytical solution of the wave field far away from the sensor.

Based on the analysis conducted in Chapter 3 and Chapter 4, the following specific conclusions which are potentially useful in designing the piezoelectric sensor SHM systems can be obtained:

(1). For the current infinite sensor system model, the strain field measured as the output signal will be disturbed by the sensor. If the sensor is perfectly bonded, the change of the load transfer will increase with the increase of loading frequency. The material combination will affect the load transfer as well. There is a critical value q^c, which is dependent on the properties of mechanical loads and materials. When $q < q^c$, the sensing ability will increase with the decrease of the thickness of the sensor; while the opposite phenomena appear when $q < q^c$. Moreover, the disturbance of the sensor will be reduced by decreasing the thickness of the sensor. Therefore, by choosing proper sensor material and geometry, as well as by controlling the mechanical loads properly, the sensing ability of the system can be promoted.

(2). For imperfectly bonded sensor system, both the sensor and the interfacial debonding will disturb the strain distribution along the sensor. The main energy of the disturbances comes from the interfacial debonding, especially for high frequency cases. The change of the strain field by different loading frequencies is more complicated for $kc > 4.0$ for currently chosen examples. $kc \leq 2.0$ will be more suitable for the sensor system with interfacial debonding. Compared with the perfect-bonding sensor system under the same loading condition and material combinations, the efficiency of dynamic load transfer is greatly reduced.

(3). The material combination of the sensor and the host structure plays a more important role in the electromechanical behavior of the imperfect piezoelectric sensor system. A softer sensor with interfacial debonding will bring more significant disturbance of the strain field along the sensor, even

under relatively low loading frequency $kc = 1.0$. Harder sensor can be chosen to reduce the influence of interfacial debonding. However, since the stress concentration around the tips of the interfacial debonding increases along with the stiffness of the sensor, attention should also be paid to make sure that the sensor will not peel off the host medium.

(4). Even for relatively low loading frequency cases, the ratio of the crack size to the sensor thickness υ is an important factor affecting the dynamic behavior of the system. The difference of the strain distribution along the sensor can be up to 20% compared with the corresponding result of perfect bonding conditions. Therefore, thinner sensor is required to assure the efficiency of the sensor, and $\upsilon > 20.0$ is more suitable for the currently selected sensor system. For the currently selected sensor with a fixed length of interfacial debonding size, $c = 2$cm for example, υ can reach 100.0 with a sensor thickness $h = 0.2$ mm. So υ from 20.0 to 100.0 is appropriate for practical applications.

(5). The wave propagation is significantly changed by the existence of interfacial debonding. For the current sensor system subjected to a harmonic wave as the load, the induced wave by the sensor will be a harmonic wave. The wave field will be changed greatly by the interfacial debonding. Along the interface, a non-vanishing surface wave can be generated. However, with the distance from the sensor increasing, it diminishes rapidly in exponential way in the hose medium. The disturbance of the interfacial debonding on the wave propagation mainly appears in the vicinity of the interface $z = 0$, in the given example, it becomes insignificant when $z < -1.0$.

5.2 Future Studies

Based on the results of the work done in this thesis, the additional investigations in a number of areas, which could be further conducted, are suggested as follows:
The simulation results obtained by using the current sensor model need to be verified by experimental work or other simulating method such as finite element

method. Proper modification of the sensor model may be needed according to the corresponding results.

(a). The current work only considered one interfacial debonding along the infinite interface. In the next step, more debonding with different sizes can be introduced. The interaction of the waves induced by the debonding need to be studied theoretically.

(b). The current two-dimensional model has its limitations. The practical SHM system is usually three dimensional, so further study and detailed simulation using 3-D model will be very important for a real SHM system.

(c). Considering the existence of interfacial debonding, design of piezoelectric sensor system will be more complicated. Extensive experimental work is desired to verify the proposed sensor testing technique, as well as the selections of the existing sensor and host materials in order to give more concrete suggestions about the optimal design of sensor systems.

(d). Piezoelectric actuator systems also need to be studied because of their wider uses in SHM techniques. Besides, embedded piezoelectric sensor/actuator systems can be expected to be studied in the similar way.

Bibliography

[1] Smith R. L., Waites C., Murgatroyd R., 1992, Assessment of NDT reliability, Proceedings of the NDT for corrosion in aerospace structures Conference, London, United Kingdom, A93-54894 24-38, p. 8.1-8.5.

[2] Wang B L, 2003, Failure Mechanics of Piezoelectric Materials and Structures (in Chinese), National Defense Industry Press, Beijing, China

[3] Park G, Farrar CR, Scalea di FL, Coccia S, 2006, Performance assessment and validation of piezoelectric active-sensors in structural health monitoring, Smart Materials & Structures, 15 (6): 1673-1683.

[4] Wang X D, Huang G L, 2006, The coupled dynamic behavior of piezoelectric sensors bonded to elastic media, Journal of intelligent material systems and structures, 17(10): 883-893.

[5] J. Sirohi, I. Chopra, 2000, Fundamental understanding of piezoelectric strain sensors, Journal of Intelligent Material Systems and Structures, 11(4):246-257.

[6] V. V. Varadan, J. Kim, V. K. Varadan, 1997, Modeling of piezoelectric sensor fidelity, IEEE Transactions of Ultrasonics, Ferroelectrics, and Frequency Control, 44(3):538-547.

[7] M. W. Lin, C. A. Rogers, 1993a, Modeling of the actuation mechanism in a beam structure with induced strain actuators, Proceedings of AIAA/ASCE/ASME/ASC 34th Structures, Structural Dynamics and Materials Conference, AIAA Inc., Washington, DC, Part VI, 3608-3617, La Jolla, CA, 19-22, April

[8] M. W. Lin, C. A. Rogers, 1993b, Actuation response of a beam structure with induced strain actuators, Adaptive Structures and Material Systems, AD 35:129-139.

[9] Charles E Seeley, 1998, Experimental investigation of composite beams with piezoelectric actuation and debonding, Smart Mater. Struct. 7: 502-511.

[10] Sun Dongchang, Tong Liyong, Satya N, Atluri, 2001, Effects of piezoelectric sensor/actuator debonding on vibration control of smart beams, International Journal of Solids and Structures, 38(50-51): 9033-9051.

[11] Sun Dongchang, Tong Liyong, 2006, Modeling and analysis of curved beams with debonded piezoelectric sensor/actuator patches, International journal of mechanical sciences, 44(8): 1755-1777.

[12] Steven A. Martin, James L. Blackshire, 2001, Effect of Adhesive Material Properties on Induced Stresses in Bonded Sensors, Review of progress in quantitative nondestructive evaluation.

[13] James L. Blackshire, Steven A. Martin, Jeong K. Na, 2007, Disbonding Effects on Elastic Wave Generation and Reception by Bonded Piezoelectric Sensor Systems, Proceedings of Conference on Sensor Systems and Networks: Phenomena, Technology, and Applications for NDE and Health Monitoring, San Diego, US, 6530.

[14] Wikipedia, Retrieved in 2009, Piezoelectricity, from: http://en.wikipedia.org/wiki/Piezoelectricity

[15] Piezo Systems Inc., Retrieved in 2009, History of Piezoelectricity, from: http://piezo.com/tech4history.html

[16] Bailey T., Hubbard J. E., 1985, Distributed piezoelectric polymer active vibration control of a cantilever beam. J. Guid. Control Dyn. 8: 605–611.

[17] Crawley E. F., Luis, J. D., 1987, Use of piezoelectric actuators as elements of intelligent structures, AIAA J. 25: 1373–1385.

[18] Edward F. Crawley, Eric H. Anderson, 1990, Detailed Models of Piezoceramic Actuation of Beams, Journal of Intelligent Material Systems and Structures, 1(1): 4-25.

[19] Im S., Atluri S.N., 1989, Effects of a Piezo-Actuator on a Finitely Deformed Beam Subjected to General Loading, AIAA Journal, 27(12):1801-1807.

[20] M.W. Lin and C.A. Rogers, 1993, Modeling of the actuation mechanism in a beam structure with induced strain actuators, Proceedings of AIAA/ASCE/ASME/ASC 34th structures, structural dynamics and materials conference, Part VI, La Jolla, CA, AIAA Inc., Washington, DC, 3608–3617.

[21] M.W. Lin and C.A. Rogers, 1993, Actuation response of a beam structure with induced strain actuators, Adaptive Structures and Material Systems AD 35, 129–139.

[22] Dimitriadis E K, Fuller C R, Rogers C A, 1991, Piezoelectric actuators for distributed vibration excitation of thin plates, J. Vib. Acoust., 113: 100-107.

[23] Dimitriadis E K, Fuller C R, Rogers C A, Roger. 1989b, Piezoelectric Actuators for Distributed Noise and Vibration Excitation of Thin Plates, Proceeding of ASME Failure Prevention and Reliability Conference, Montreal, 223-233.

[24] John S. Richard, Harley H. Cudney, 1993, Modeling multiple-layer piezoelectric actuators in active structural control, Proceedings of SPIE on Smart Structures and Materials, Albuquerque, NM, USA, 1916: 231.

[25] Mindlin R. D., 1952, Forced thickness-shear and flexural vibration of piezoelectric crystal plates, J. Appl. Phys., 23:83-88.

[26] Tiersten H. F., Mindlin R. D., 1962, Forced vibrations of piezoelectric crystal plates, Quat. Appl. Math., 20:107-119.

[27] Mindlin R. D., 1972, High frequency vibrations of piezoelectric crystal plates, Int. J. Solids. Struct., 8:895-906.

[28] Mindlin R. D., 1984, Frequencies of piezoelectrically forced vibrations of electrodes doubly rotated quartz plates, Int. J. Solids. Struct., 20:141-157.

[29] E. Crawley and K.B. Lazarus, 1991, Induced strain actuation of isotropic and anisotropic plates, AIAA Journal, 29: 944–951.

[30] Wang B.T., Rogers C., 1991, A Laminate plate theory for spatially distributed induced strain actuators, Journal of Composite Materials, 25: 433-452.

[31] Rahmoune M., Benjeddou A., Ohayon R., Osmont D., 1998, New thin piezoelectric plate models, Journal of intelligent material systems and structures, 9(12): 1017-1029.

[32] Tzou H. S., 1989, Distributed sensing and controls of flexible plates and shells using distributed piezoelectric elements, Journal of wave-material interaction, 4: 1-3.

[33] Tzou H. S., Gadre M., 1989, Theoretical analysis of a multi-layered thin shell coupled with piezoelectric shell actuators for distributed vibration controls, Journal of Sound and Vibration

[34] Tzou H. S, Y Bao, 1994, Modeling of thick anisotropic composite triclinic piezoelectric shell transducer laminates, Smart Mater. Struct. 3: 285-292.

[35] Zhu X, Wang Q, Meng Z, 1995, A functionally gradient piezoelectric actuator prepared by power metallurgical process in PNN-PZ-PT system, Journal of Material Science Letter, 14: 516-518.

[36] Wu C M, Kahn M, Moy W, 1996, Piezoelectric ceramics with functionally gradients: a new approach in material design, Journal of American Ceramic Society, 79: 809-812.

[37] Qiu J, Tani J, Soga T, 1996, Smart functionally graded material without bending deformation, Proceedings of the 4th international symposium on functionally graded materials, FGM'96: 773-780.

[38] Ootao Y, Tanigawa Y, 2000, Three-dimensional piezoelasticity in functionally graded rectangular plate bonded to a piezoelectric plate, Int. J. Solids Structures, 37: 4377-4401.

[39] Almajid A, Taya M, Hudnut S, 2001, Analysis of out-of-plane displacement and stress field in a piezoelectric plate with functionally graded microstructure, Int. J. Solids Structures,38: 3377-3392.

[40] He X Q, Ng T Y, Sivashanker S, Liew K M, 2001, Active control of FGM plates with integrated piezoelectric sensors and actuators, Int. J. Solids Structures, 38(9): 1641-1655.

[41] Wang B L, Noda N, 2001, Design of a smart functionally graded piezothemoelastic structure, Smart Materials and Structures, 10(2): 189-193.

[42] Wang B L, Noda N, 2001, Thermally induced fracture of a smart functionally graded composite structure, Theoretical and applied fracture mechanics, 35(2): 93-109.

[43] Wang B L, Noda N, 2001, Axisymmetric deformation of piezoelectric multilayers, Philosophical Magazine Part A, 81(4): 1009-1019.

[44] Chen W Q, Wang L Z, 2002, Free vibrations of functionally graded piezoceramic hollow spheres with radial polarization, J. Sound Vib., 251(1): 103-114.

[45] Nowachi W. 1978, Some general theorems of thermopiezoelectricity, Journal of Thermal Stresses, 1: 171-182.

[46] Chandrasekharaiah D. S., 1988, A generalized linear thermoelasticity theory of piezoelectric media, Acta Mech., 71: 39-49.

[47] Ding H, Guo F, Hou P, 2000, A general solution for piezothermoelasticity of transversely isotropic piezoelectric materials and its applications, International Journal of Engineering Science, 38: 1415-1440.

[48] Tauchert T R, 1992, Piezothermoelastic behavior of the laminated plate, Journal of Thermal Stresses, 15: 25-37.

[49] Ashida F., Tauchert T.R, Noda N, 1993, Response of a piezothermoelastic plate of crystal class 6 mm subject to axisymmetric heating, International Journal of Engineering Science, 31: 373-384.

[50] Choi J, Ashida F, Noda N, 1995, Transient piezothermoelasticity of a hexagonal plate class 6 mm, Achieve of Applied Mechanics, 65: 24-37.

[51] Qin Q H, 2000, General solutions for thermopiezoelectrics with various holes under thermal loading, International Journal of Solids and Structures, 37: 5561-5578.

[52] Y. W. Kwon and H. Aygunes, 1996, Dynamic finite element analysis of laminated beams with delamination cracks using contact-impact conditions, Computers & Structures, 58(6): 1161-1169.

[53] Corrado Maurini, Joël Pouget, Francesco dell'Isola, 2006, Extension of the Euler–Bernoulli model of piezoelectric laminates to include 3D effects via a mixed approach, Computers & Structures, 84: 1438-1458.

[54] Allik, H., T. J. R. Hughes, 1970, Finite Element Method for Piezoelectric Vibration, International Journal for Numerical Methods in Engineering, 2:151–157.

[55] H. S. Tzou , C. I. Tseng , H. Bahrami, 1994，A thin piezoelectric hexahedron finite element applied to design of smart continua, Finite Elements in Analysis and Design, 16(1): 27-42.

[56] Benjeddou A., M. A. Trindade, R. Ohayon, 1998, A new shear actuated smart structure beam element, AIAA 98: 1922.

[57] Heyliger P., Ramirez G., Saravanos D., 1994, Coupled discrete-layer finite elements for laminated piezoelectric plates, Communications in numerical methods in engineering, 10(12): 971-981.

[58] M.A. Moetakef, K.L. Lawerence, S.P. Joshi, P.S. Shiakolas, 1995, Closed form expressions for higher order electroelastic tetrahedral elements, AIAA J., 33: 136-142.

[59] C.C. Wu, K.Y. Sze, Y.Q. Huang, 2001, Numerical solutions on fracture of piezoelectric materials by hybrid element, Int. J. Solids Struct., 38: 4315-4329.

[60] K.Y. Sze, 1992, Efficient formulation of robust hybrid elements using orthogonal stress/strain interpolants and admissible matrix formulation, Int. J. Numer. Methods Eng., 35: 1-20.

[61] Lesieutre, George A., 1998, Vibration damping and control using shunted piezoelectric materials, SHOCK VIB DIG., 30(3): 187-195.

[62] Preumont, A., 1997, Vibration Control of Active Structures - An Introduction, Kluwer Academic Publishers.

[63] K. Chandrashekhara, S. Varadarajan, 1997, Adaptive Shape Control of Composite Beams with Piezoelectric Actuators, Journal of Intelligent Material Systems and Structures, 8(2): 112 - 124.

[64] Victor Giurgiutiu, Andrei Zagrai, Jing Jing Bao, 2002, Piezoelectric Wafer Embedded Active Sensors for Aging Aircraft Structural Health Monitoring, Structural Health Monitoring, 1(1): 41-61.

[65] Chee-Kiong SOH, Yaowen YANG, 2007, Integrating Evolutionary Programming and Electro-Mechanical Impedance Method for Damage Identification, Procedinging of ASCE(American Society of Civil Engineers)

International Workshop on Computing in Civil Engineering; Pittsburgh, PA(US), 24-27, July.

[66] Ajay Raghavan, Carlos E. S. Cesnik, 2004, Modeling of piezoelectric-based Lamb wave generation and sensing for structural health monitoring, Proc. SPIE, 5391: 419.

[67] Deng W, Meguid S A, 1998, Analysis of conducting rigid inclusion at the interface of two dissimilar piezoelectric materials, J. Appl. Mech., (ASME) 65:76-84.

[68] Beom H G, Auluri S N, 1996, Near-tip fields and intensity factors for interfacial cracks in dissimilar anisotropic piezoelectric media, Int. J. Fracture, 75: 163-183.

[69] Dongchang Sun; Liyong Tong, 2002, Modeling and analysis of curved beams with debonded piezoelectric sensor/actuator patches, International Journal of Mechanical Sciences, 44(8): 1755-1777.

[70] Yang Jiashi, 2007, Thickness-twist edge modes in a semi-infinite piezoelectric plate of crystals with 6mm symmetry, IEEE Transactions on Ultrasonics, Ferroelectrics, and Frequency Control, 54(2): 220-221.

[71] William H Prosser, 1996, Advanced AE techniques in composite material research, 1996, Journal of Acoustic Emission, 14(3-4): S1-S11.

[72] Kromine A. K, Fomitchov P. A, Krishnaswamy S., Achenbach J. D, 2000, Laser ultrasonic detection of surface breaking discontinuities: scanning laser source technique, Materials Evaluation, 58(2):173-177.

[73] Fu-Kuo Chang, 2000, Structual Health Monitoring, Air Force, Office of Scientific Research, United States.

[74] X Lin, F G Yuan, 2001, Diagnostic Lamb waves in an integrated piezoelectric sensor/actuator plate: analytical and experimental studies, Smart Mater. Struct. 10: 907-913.

[75] MONKHOUSE R S C, WILCOX P D, CAWLEY P, 1997, Flexible interdigital PVDF transducers for the generation of Lamb waves in structures, Ultrasonics, 7.

[76] MONKHOUSE R S C, WILCOX P D, 2000, The rapid monitoring of the structures using interdigital Lame wave transducers, Smart Materials and Structures, 5.

[77] J. P. Lynch , A. Sundararajan , H. Sohn , G. Park , C. Farrar , K. H. Law, 2004, Embedding Actuation Functionalities in a Wireless Structural Health Monitoring System, Proceedings of the International Workshop on Smart Materials and Structures Technology.

[78] X. D. Wang, G. L. Huang, 2001, Wave Propagation in Electromechanical Structures: Induced by Surface-Bonded Piezoelectric Actuators, Journal of Intelligent Material Systems and Structures, 12(2): 105-115.

[79] L. Han, X. D. Wang, Y. Sun, 2008, The effect of bonding layer properties on the dynamic behaviour of surface-bonded piezoelectric sensors, International Journal of Solids and Structures, 45(21): 5599-5612.

[80] J. D. Achenbach, 1973, Wave propagation in elastic solids, American Elsevier Publishing Company, Inc. New York, N.Y. USA

[81] Y. Eugene Pak, 1990, Crack Extension Force in a Piezoelectric Material, J. Appl. Mech., 57(3): 647

[82] Jaehwan Kim, Vasundara V. Varadan, Vijay K. Varadan, 1997, Finite element modelling of structures including piezoelectric active devices, International Journal for Numerical Methods in Engineering, 40(5): 817 – 832

[83] C. K. Lee, F. C. Moon, 1989, Laminated piezopolymer plates for torsion and bending sensors and actuators, Journal of the Acoustic Society of America, 85(6): 2432-2439.

Appendix A

Plane Harmonic Waves in Elastic Half-spaces

A plane harmonic displacement wave propagating with phase velocity c in a direction defined by the unite propagation vector $\vec{p}$ is represented by:

$$\vec{u} = A\vec{d}e^{i\eta} \tag{A.1}$$

where $\eta = k(\vec{x} \cdot \vec{p} - ct)$, A and k as the amplitude and the wave number, respectively.

The plane harmonic waves are divided into two types based on the directions of motion and wave propagation:

Longitudinal wave, for which $\vec{d} = \pm\vec{p}$ and $c = c_L$;

Transverse wave, for which $\vec{d} \cdot \vec{p} = 0$ and $c = c_T$.

For in-plane motions, the incident as well as the reflected and refracted waves can be obtained, denoted by:

$$\vec{u}^{(n)} = A_n \vec{d}^{(n)} e^{i\eta_n} \tag{A.2}$$

where

$$\eta_n = k_n (\vec{x} \cdot \vec{p}^{(n)} - c_n t) \tag{A.3}$$

Different values of the index number n serve to label the various types of waves that occur. The value $n = 0$ is assigned for the incident wave, with

$$\vec{p}^{(0)} = \sin\theta_0 \cdot \vec{i}_1 + \cos\theta_0 \cdot \vec{i}_2. \tag{A.4}$$

where θ_0 is the phase angle of the incident wave.

For an incident longitudinal wave, we have:

$$\vec{d}^{(0)} = \vec{p}^{(0)}, \qquad c_0 = c_L. \tag{A.5}$$

For an incident transverse wave, we have:

$$\vec{d}^{(0)} \cdot \vec{p}^{(0)} = 0, \qquad c_0 = c_T. \tag{A.6}$$

The reflected waves may be both longitudinal and transverse waves. The reflected longitudinal waves and the reflected transverse waves are labeled by $n = 1$ and $n = 2$, respectively. The expressions are as follows:

Reflected longitudinal wave:

$$\vec{p}^{(1)} = \sin\theta_1 \cdot \vec{i}_1 - \cos\theta_1 \cdot \vec{i}_2, \qquad \vec{d}^{(1)} = \vec{p}^{(1)}, \qquad c_1 = c_L \quad \text{(A.7)}$$

Reflected transverse wave:

$$\vec{p}^{(2)} = \sin\theta_2 \cdot \vec{i}_1 - \cos\theta_2 \cdot \vec{i}_2, \qquad \vec{d}^{(2)} = \vec{i}_3 \otimes \vec{p}^{(2)}, \qquad c_2 = c_T \quad \text{(A.8)}$$

And the unknown amplitude A_1, A_2 and phase angle θ_1, θ_2 of the reflected waves can be solved with the stress and displacement boundary conditions along the joined surfaces between the two elastic half-spaces. For a plane longitudinal waves which propagates in an elastic half space with a free surface, the following conclusions can be obtained:

$$k_0 \sin\theta_0 = k_1 \sin\theta_1 = k_2 \sin\theta_2 = k = \text{Apparent wave number} \qquad \text{(A.9)}$$

$$k_0 c_L = k_1 c_L = k_2 c_T = \omega = \text{Circular frequency.} \qquad \text{(A.10)}$$

These results provide, in turn, the following relations:

$$k_1 = k_0 \qquad \text{(A.11)}$$

$$\frac{k_2}{k_0} = \frac{c_L}{c_T} = \kappa \qquad \text{(A.12)}$$

$$\theta_1 = \theta_0 \qquad \text{(A.13)}$$

$$\sin\theta_2 = \kappa^{-1} \sin\theta_0. \qquad \text{(A.14)}$$

The material constant κ is defined by:

$$\kappa = \left[\frac{2(1-v)}{1-2v} \right]^{1/2} \qquad \text{(A.15)}$$

where v is Poisson's ratio.

The relations of the amplitude of reflected waves and the incident wave are:

$$\frac{A_1}{A_0} = \frac{\sin 2\theta_0 \sin 2\theta_2 - \kappa^2 \cos^2 2\theta_2}{\sin 2\theta_0 \sin 2\theta_2 + \kappa^2 \cos^2 2\theta_2} \qquad \text{(A.16)}$$

$$\frac{A_2}{A_0} = \frac{2\kappa \sin 2\theta_0 \cos 2\theta_2}{\sin 2\theta_0 \sin 2\theta_2 + \kappa^2 \cos^2 2\theta_2}. \qquad \text{(A.17)}$$

Therefore, the displacement field in the elastic half space can be obtained by superposing the displacements induced by the incident as well as the reflected waves, which is:

$$\vec{u} = \vec{u}^{(0)} + \vec{u}^{(1)} + \vec{u}^{(2)} \tag{A.18}$$

with which the corresponding components of the strain and stress field inside the half space can be obtained.